A numerical simulation of unsteady flow in a two-dimensional collapsible channel

By X. Y. LUO and T. J. PEDLEY†

Department of Applied Mathematical Studies, The University of Leeds, Leeds LS2 9JT, UK

The collapse of a compressed elastic tube conveying a flow occurs in several physiological applications and has become a problem of considerable interest. Laboratory experiments on a finite length of collapsible tube reveal a rich variety of self-excited oscillations, indicating that the system is a complex, nonlinear dynamical system. Following our previous study on steady flow in a two-dimensional model of the collapsible tube problem (Luo & Pedley 1995), we here investigate the instability of the steady solution, and details of the resulting oscillations when it is unstable, by studying the time-dependent problem. For this purpose, we have developed a time-dependent simulation of the coupled flow–membrane problem, using the Spine method to treat the moving boundary and a second-order time integration scheme with variable time increments.

It is found that the steady solutions become unstable as tension falls below a certain value, say T_u, which decreases as the Reynolds number increases. As a consequence, steady flow gives way to self-excited oscillations, which become increasingly complicated as tension is decreased from T_u. A sequence of bifurcations going through regular oscillations to irregular oscillations is found, showing some interesting dynamic features similar to those observed in experiments. In addition, vorticity waves are found downstream of the elastic section, with associated recirculating eddies which sometimes split into two. These are similar to the vorticity waves found previously for flow past prescribed, time-dependent indentations. It is speculated that the mechanism of the oscillation is crucially dependent on the details of energy dissipation and flow separation at the indentation.

As tension is reduced even further, the membrane is sucked underneath the downstream rigid wall and, although this causes the numerical scheme to break down, it in fact agrees with another experimental observation for flow in thin tubes.

1. Introduction

Flow in thin-walled collapsible tubes has numerous applications to physiology and to medical devices. Laboratory experiments have found a rich variety of self-excited oscillations in such flow systems, which have stimulated great interest among researchers in biomathematics and bioengineering. In particular, Bertram, Raymond & Pedley (1990,1991) present results which reveal an interesting bifurcation structure leading, almost certainly, to chaotic motion in some parts of parameter space. Numbers of theories, most of them one-dimensional, have been put forward to explain the physical mechanisms responsible for the generation of the self-excited oscillations (e.g. Reyn 1974; Shapiro 1977; Cancelli & Pedley 1985; Jensen 1992; Matsuzaki &

† Present address: Department of Applied Mathematics and Theoretical Physics, University of Cambridge, Silver Street, Cambridge CB3 9EW, UK.
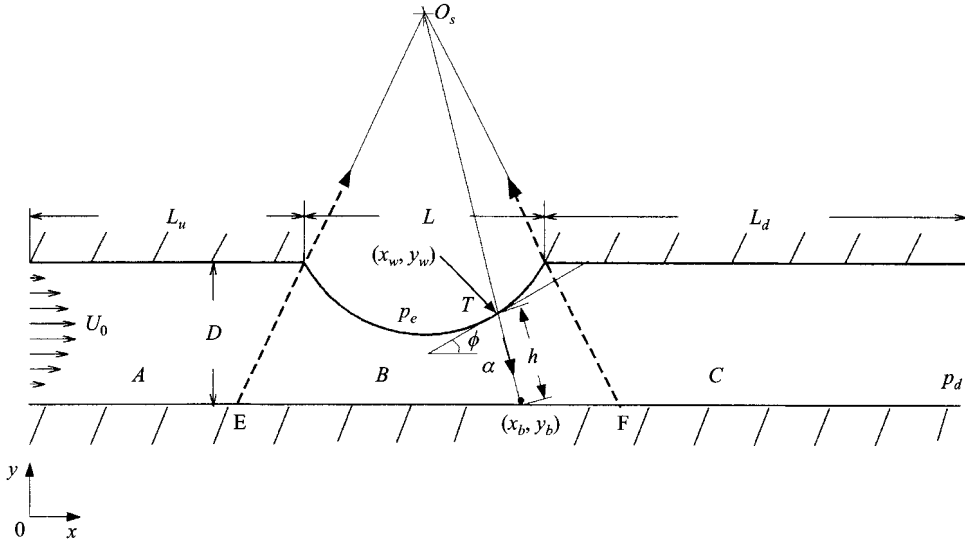
FIGURE 1. Two-dimensional flow configuration. Steady Poiseuille flow with average velocity U_0 entering upstream; p_d is pressure at the downstream end of the channel, p_e is the external pressure and T is the tension in the membrane. For explanation of other symbols, see text.

Matsumoto 1989; Pedley 1992). However, owing to the great complexity of the system, involving three-dimensional dynamic behaviour and fluid–structure interactions, these mechanisms are still not fully understood.

From the mathematical point of view, a self-excited oscillation can arise only when a steady solution fails to exist or becomes unstable in a system with constant control parameters. Hence it is essential to investigate the existence and the stability of the steady flow in a rationally described model, including important effects such as the nonlinearity of the flow and wall dynamics.

Previous studies have been carried out on two-dimensional steady flow in a rigid, parallel sided channel in which part of one wall is replaced by a membrane under tension (figure 1). These studies mainly concentrated on the existence of steady solutions(Lowe & Pedley 1994; Rast 1994; Luo & Pedley 1995). It was found that in the given range of Reynolds number and transmural pressure, although a steady flow solution should exist for all values of longitudinal tension according to one-dimensional analytic models, the numerical simulation could only achieve these solutions for a sufficiently large tension. Because the 'critical' value of tension for a given Reynolds number differed in the two finite-Reynolds-number computations (Rast 1994; Luo & Pedley 1995), we are now convinced that this failure to find a solution represents a numerical breakdown. The numerical failure could be caused either by an inadequate mesh which fails to cope with the extreme wall shape (too close to the opposite wall or too steep in the downstream region), or by the fact that the problem becomes quite stiff when the tension is very low (and hence the wall curvature becomes very large in the membrane equation).

In this paper, we study unsteady flow in a two-dimensional channel using the finite element method, aiming to investigate (*a*) the stability of those steady solutions found in the previous study (Luo & Pedley 1995), and (*b*) the self-excited oscillations that develop after the steady solutions become unstable.

We shall indeed find evidence of a sequence of bifurcations, similar to some of these observed experimentally by Bertram *et al.* (1990,1991), and suggestive of period-

doubling which is one of the conventional routes to chaos. Another important finding is that a train of *vorticity waves* is generated and propagates downstream during each cycle of oscillation. This is not unexpected, because such waves have previously been experimentally observed downstream of an indentation in a two-dimensional channel which moves in and out in a prescribed way (Pedley & Stephanoff 1985), but this is the first time that they have been found in a coupled flow–structure problem. The phase relation between the waves and the wall motion supports the proposal of Cancelli & Pedley (1985) that the unsteady process of flow separation and the associated energy loss are important parts of the oscillation mechanism.

2. The mathematical model

2.1. *Assumptions*

The flow configuration is shown in figure 1. The rigid channel has width D; one part of the upper wall is replaced by an elastic membrane subjected to an external pressure p_e. Steady Poiseuille flow with average velocity U_0 is assumed at the entrance. The flow is incompressible and laminar, the fluid having density ρ and viscosity μ. The longitudinal tension $\bar{T}$ is taken to be constant, i.e. variations due to the wall shear stress or the overall change of the membrane length are considered to be small relative to the initial stretching tension. Further, we assume that the inertia of the membrane is negligible, an assumption that is likely to be valid for rubber-like membranes if the flowing fluid is water, but questionable if it is air (see below).

2.2. *Governing equations*

The dimensionless momentum and the continuity equations are

$$\left(\frac{\partial u_i}{\partial t} + u_j u_{i,j} \right) = -p_{,i} + \frac{1}{Re} u_{i,jj}, \tag{1}$$

$$u_{i,i} = 0, \qquad i = 1, 2 \tag{2}$$

where $Re = U_0 D \rho / \mu$ is the Reynolds number. The membrane equation is

$$\sigma_n - p_e = -\kappa T \tag{3}$$

where σ_n is the fluid stress acting on the membrane in the normal direction, p_e is the external pressure, T is the longitudinal tension, and κ is the wall curvature which can be expressed as the derivative along the membrane of the angle made by the tangent to the elastic boundary with the x-axis:

$$\kappa = \frac{\mathrm{d}\phi}{\mathrm{d}s}. \tag{4}$$

If wall inertia were included, a term ma would be added to the right-hand side of (3), where a is the (dimensionless) acceleration of the wall in the normal direction and m is the ratio of membrane to fluid density, multiplied by the ratio of membrane thickness to D. The latter ratio is assumed to be small, while the former is $O(1)$ when the fluid is water, so in that case it is reasonable to neglect wall inertia.

All the variables are non-dimensionalized as

$$\begin{aligned} u_i &= \bar{u}_i/U_0 \quad (i = 1, 2), \quad \sigma = \bar{\sigma}/\rho U_0^2, \\ p &= \bar{p}/\rho U_0^2, \quad T = \bar{T}/\rho U_0^2 D, \\ x &= \bar{x}/D, \quad y = \bar{y}/D, \quad t = \bar{t} U_0/D, \end{aligned}$$

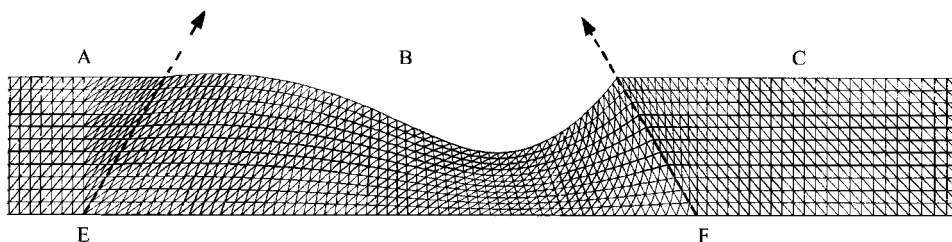where variables with an overbar denote dimensional quantities.

FIGURE 2. Part of a typical adaptive mesh of the flow domain; there are 5060 triangular elements with 10603 nodes, with 22×124 movable nodes located in section B.

2.3. Boundary conditions

The boundary conditions imposed on the flow domain are

inlet flow: $u = 6y(1 - y), v = 0$ at $x = 0, 0 \leqslant y \leqslant 1$;

rigid walls: $u = v = 0$ at $y = 0, 0 \leqslant x \leqslant L_u + L + L_d$,

                                       at $y = 1, 0 \leqslant x \leqslant L_u$ and

                                     $L_u + L \leqslant x \leqslant L_u + L + L_d$;

elastic section: $u(t) = u_w(t); v(t) = v_w(t)$ at $x = x_w(t); y = y_w(t)$;

outflow: $\sigma_t = 0, \sigma_n = -p_d$ at $x = L_u + L + L_d, 0 \leqslant y \leqslant 1$,

where p_d is the downstream pressure, chosen to be zero here. The velocity is prescribed on all boundaries except at the outflow, which is taken to be stress free, and on the elastic section, where x_w and y_w are the coordinates of a general point of the membrane, given by

$$x_w = x_b + \alpha_x h(t) , \; y_w = y_b + \alpha_y h(t).$$

Here h is the extra unknown describing the moving boundary, also called the spine height (see figure 1, figure 2 and §3.1), x_b, y_b are the coordinates of fixed base points along the wall section EF, and α_x, α_y are the components of the direction vector α of spine h. α is fixed in time but varies along the section EF, giving a set of spines with different orientations.

For values of the Reynolds number much greater than one, as in most cases examined here, the stress-free conditions are the best choice for simulating the corresponding experiments in which the downstream pressure is fixed, though care must be taken to make L_d sufficiently large.

It is the velocity boundary conditions on the elastic section that make this problem different from a free-surface problem under surface tension, which otherwise obeys the same governing equations (1)–(3). To apply these conditions, we have to find out in which direction the material points move on the wall. However, this is not known in our model since a membrane equation is used to describe the wall mechanics and individual elements of the membrane are not tracked. For simplicity, therefore, we make a further *ad hoc* assumption: we assume that the wall points always move in the direction normal to its surface. This is approximately consistent with the constant tension assumption used here and is in fact exact if the wall shape remains circular.

Another possible assumption that has frequently been used in modelling flow with compliant walls (Kramer 1962; Carpenter & Garrad 1986; Riley, Gad el Hak & Metcalfe 1988; Ehrenstein & Koch 1989) is to assume that the points move along the vertical, y-direction. However, this is a good approximation only if the deformation of the wall is very small, whereas we are interested in cases for which the wall can experience quite large deformation. Therefore this assumption is not made in our

model, except that comparison of the two approximations will be made for two cases below, showing the results not to be significantly influenced by the choice of boundary condition.

3. Methods

We adopt the simultaneous approach used by Rast (1994) for the steady flow computation. The idea is to solve the incompressible Navier–Stokes equations (1) and (2) together with the membrane equation (3) on the elastic boundary to determine simultaneously both the flow field and the domain shape, instead of alternating between fluid and wall equations. The elastic boundary is parameterized in terms of spine heights in a manner similar to that which has been used successfully in studies of viscous free-surface flows (Silliman 1979; Ruschak 1980; Saito & Scriven 1981). The differences in the present implementation are that the membrane curvature equation (3), with the form (4) of the wall curvature, is used to determine the spine heights. The method for the steady flow is discussed in detail by Rast (1994); here we will concentrate on the unsteady flow simulation.

3.1. *The adaptive mesh*

The flow domain is divided into three six-node triangular finite element subdomains, figure 2. Subdomains A and C have nodes fixed in space, while subdomain B, under the elastic section, contains the mesh with moving nodes. The angles of the two edges of subdomain B are chosen to allow a rather steep slope of the membrane near the downstream end, as was observed in the steady flow simulations when tension is small (Rast 1994; Luo & Pedley 1995). The shape of this subdomain depends on the unknown elastic boundary. The elemental nodes under the elastic section lie along the spines which emanate from a fixed origin O_s. Each spine k is defined by the Cartesian coordinates of its base point, x_b^k and $y_b^k(=0)$, and the direction from that point to the origin. The position of node i on spine k is given in terms of a fixed fraction ω_i^k of the spine height h^k as

$$x_i^k = x_b^k + \alpha_x^k \omega_i^k h^k, \qquad y_i^k = y_b^k + \alpha_y^k \omega_i^k h^k,$$

where $\alpha = (\alpha_x^k, \alpha_y^k)$ is the direction vector of spine k, and the spine height is simply the distance from the spine base to the elastic surface in the direction of α. Each spine height is an unknown in the problem and is to be determined as part of the solution.

3.2. *Time derivatives*

The time derivatives appearing in (1) are the Eulerian time derivatives, i.e. the nodal velocity field must be defined for nodes fixed in space. However, the technique for parameterization of the moving surface is such that the nodes are constrained to move along a fixed line in space–a mixed Eulerian–Lagrangian formulation. Thus the time derivatives in (1) must be transformed to time derivatives which follow the moving nodes along these lines. Denoting by $\delta/\delta t$ the time derivatives following a moving node, the relation between $\delta/\delta t$ and $\partial/\partial t$, the Eulerian time derivative, is given by

$$\frac{\delta \boldsymbol{u}}{\delta t} = \frac{\partial \boldsymbol{u}}{\partial t} + \dot{\boldsymbol{x}}^k \cdot \nabla \boldsymbol{u} \tag{5}$$

where $u = \{u, v\}$ and

$$\dot{x}^k = \alpha^k \omega^k \frac{dh^k}{dt} .$$

Therefore the time derivatives in (1) become

$$\frac{\partial u}{\partial t} = \frac{\delta u}{\delta t} - \left(\alpha_x^k \frac{\partial u}{\partial x} + \alpha_y^k \frac{\partial u}{\partial y} \right) \omega^k \frac{dh^k}{dt},$$

$$\frac{\partial v}{\partial t} = \frac{\delta v}{\delta t} - \left(\alpha_x^k \frac{\partial v}{\partial x} + \alpha_y^k \frac{\partial v}{\partial y} \right) \omega^k \frac{dh^k}{dt}$$

where the second part of these expressions represents the movement of the nodes in the moving domain.

3.3. Finite element algorithm

3.3.1. Space integration

The finite element implementation now follows fairly straightforwardly. Within each element, the variables are expanded isoparametrically in area coordinates, (ζ, η), employing a mixed interpolation, with u, v, x, and y sharing quadratic and p linear expansions:

$$u = \sum_{i=1}^{6} u_i N_i(\zeta, \eta), \quad v = \sum_{i=1}^{6} v_i N_i(\zeta, \eta), \quad p = \sum_{i=1}^{3} p_i L_i(\zeta, \eta),$$

$$x = \sum_{i=1}^{6} x_i(h, \theta) N_i(\zeta, \eta), \quad y = \sum_{i=1}^{6} y_i(h, \theta) N_i(\zeta, \eta)$$

where L_i and N_i are linear and quadratic shape functions respectively, and θ is the angle of a spine with the vertical (Rast 1994). Equations determining the nodal values of u, v, p and h are derived by the Galerkin method of weighted residuals. The finite element equation

$$M \frac{dU}{dt} + K(U)U - F = R = 0, \tag{6}$$

represents a discrete-space, continuous-time approximation to (1)–(3), where U is the global vector of unknowns $(u_i, v_i, p_j,$ and $h_k)$, with $i = 1$–N, $j = 1$–M, $k = 1$–N_s, where N is the total number of velocity nodes, M the total number of pressure nodes, and N_s the total number of spine heights. R is the overall residual vector which should be zero for an exact solution. Here

$$R = (R_x, R_y, R_c, R_e)^T,$$

where the subscripts x, y, c, and e indicate the corresponding residuals of the x and y-momentum, continuity, and membrane equations, respectively. For each element, expressions for these quantities are

$$R_c^k = \sum_{i=1}^{6} u_i \int \int L_k \frac{\partial N_i}{\partial x} dx dy + \sum_{i=1}^{6} v_i \int \int L_k \frac{\partial N_i}{\partial y} dx dy = 0,$$

$$R_e^l = -P_e \int N_l ds + \sum_{j=2}^{3} P_j \int N_l L_j ds + T \sum_{j=1}^{3} \int N_l L_j \frac{\partial \phi}{\partial s} ds = 0,$$

$$R_x^l = \sum_{i=1}^{6} \frac{\delta u_i}{\delta t} \int \int N_i N_l \mathrm{d}x\mathrm{d}y - \sum_{k=1}^{3}\sum_{i=1}^{6} u_i \omega^k \frac{\mathrm{d}h^k}{\mathrm{d}t} \int \int N_i N_l \left(\alpha_x^k \frac{\partial N_i}{\partial x} + \alpha_y^k \frac{\partial N_i}{\partial y} \right) \mathrm{d}x\mathrm{d}y$$

$$+ \sum_{i=1}^{6}\sum_{j=1}^{6} u_i u_j \int \int N_i N_l \frac{\partial N_i}{\partial x} \mathrm{d}x\mathrm{d}y + \sum_{i=1}^{6}\sum_{j=1}^{6} u_i v_j \int \int N_i N_l \frac{\partial N_i}{\partial y} \mathrm{d}x\mathrm{d}y$$

$$- \sum_{j=1}^{3} P_j \int \int L_j \frac{\partial N_l}{\partial x} \mathrm{d}x\mathrm{d}y + \frac{1}{Re} \sum_{i=1}^{6} u_i \int \int \frac{\partial N_i}{\partial x} \frac{\partial N_l}{\partial x} \mathrm{d}x\mathrm{d}y$$

$$+ \frac{1}{Re} \sum_{i=1}^{6} u_i \int \int \frac{\partial N_i}{\partial y} \frac{\partial N_l}{\partial y} \mathrm{d}x\mathrm{d}y + \sum_{j=1}^{3} P_j \int N_l L_j n_x \mathrm{d}s$$

$$- \frac{1}{Re} \sum_{i=1}^{6} u_i \int N_l \frac{\partial N_i}{\partial x} n_x \mathrm{d}s - \frac{1}{Re} \sum_{i=1}^{6} u_i \int N_l \frac{\partial N_i}{\partial y} n_y \mathrm{d}s = 0,$$

with $k = 1\text{--}3$ for pressure on the vertices and $l = 1\text{--}6$ for velocities on all nodes within each element. R_y^l can be written in a similar form. Boundary elements are oriented so that three nodes ($l = 3$, 5 and 2) lie along the elastic membrane. The coordinates of all nodes below the elastic boundary depend on the boundary position, therefore ϕ, $\hat{n}$, $\mathrm{d}s$, and the Jacobian of the coordinate transformation for those elements which contain these nodes, are all functions of x and y, hence of the spine height h.

Boundary conditions are imposed in a standard way and the integrals are evaluated at Gauss points within each element. However, problems arise when we apply the no-slip conditions on the elastic boundary. Since normal movement is assumed for points on the membrane, the velocities u_w, v_w are related to the change of spine height through the following equations:

$$u_w^k = (\hat{\alpha}^k \cdot \hat{n}^k) \frac{\mathrm{d}h^k}{\mathrm{d}t} n_x^k, \tag{7}$$

$$v_w^k = (\hat{\alpha}^k \cdot \hat{n}^k) \frac{\mathrm{d}h^k}{\mathrm{d}t} n_y^k \tag{8}$$

where the normal vector $\hat{n}^k$ is defined on a node associated with the spine k . On the other hand, the normal vector $\hat{n} = (n_x, n_y)$ in the integrals of $\boldsymbol{R}$ in (6) is not uniquely defined at the nodes. Thus we have to interpolate the nodal $\hat{n}^k$ from $\hat{n}$. An appropriate (and unique) normal direction at a node may be determined by invoking mass conservation for an incompressible fluid, $\int \int u_{i,i} \mathrm{d}x\mathrm{d}y = 0$ (Engelman, Sani & Gresho 1982), which can be manipulated to give

$$n_x^k = \frac{1}{n^k} \int \int \frac{\partial N_k}{\partial x} \mathrm{d}x\mathrm{d}y, \, n_y^k = \frac{1}{n^k} \int \int \frac{\partial N_k}{\partial y} \mathrm{d}x\mathrm{d}y,$$

where

$$n^k = \left[\left(\int \int \frac{\partial N_k}{\partial x} \mathrm{d}x\mathrm{d}y \right)^2 + \left(\int \int \frac{\partial N_k}{\partial y} \mathrm{d}x\mathrm{d}y \right)^2 \right]^{1/2},$$

and N_k is the shape function at the node associated with the spine k. Applying Green's theorem to the above equations, we obtain

$$n_x^k = \frac{1}{n^k} \int N_k n_x \mathrm{d}s, \quad n_y^k = \frac{1}{n^k} \int N_k n_y \mathrm{d}s, \tag{9}$$

where the integral is defined along the arclength of the membrane. Note that equation (9) is the relation between the nodal normal components n_x^k, n_y^k and the components n_x, n_y of the normal that are defined at the Gauss points.

3.3.2. Time integration

Equation (6) is integrated with time by using an implicit finite difference scheme, i.e.

$$M(U_{n+1})\dot{U}_{n+1} + K(U_{n+1})U_{n+1} - F(U_{n+1}) = R_{n+1}(U_{n+1}, U_n) = 0 \qquad (10)$$

where $\dot{U}_{n+1}$ is approximated by a backward-Euler first-order scheme for the first 3–4 steps with constant time increment, i.e.

$$\dot{U}_{n+1} = \frac{U_{n+1} - U_n}{dt}. \qquad (11)$$

This is followed by a second-order predictor-corrector scheme with a variable time step dt_n. First, the second-order-accurate Adams–Bashforth explicit approximation

$$U_{n+1}^p = U_n + \frac{dt_n}{2}\left[\left(2 + \frac{dt_n}{dt_{n-1}}\right)\dot{U}_n - \frac{dt_n}{dt_{n-1}}\dot{U}_{n-1}\right] \qquad (12)$$

is used as the predictor at time step $n + 1$, which gives the truncation error

$$U_{n+1}^p - U(n + 1) = -\frac{1}{12}\left(2 + 3\frac{dt_{n-1}}{dt_n}\right)(dt_n)^3\dddot{U}_{n+1} + O(dt_n)^4. \qquad (13)$$

Since this is an explicit formula, it is only applied to velocity components and spine height, not to the pressure unknown whose time derivative does not appear in the equations. The predictor of pressure is therefore simply the solution from the previous time step, i.e. a zeroth-order predictor is used.

Second, the corrector step uses the non-dissipative, completely stable trapezoid rule, i.e. solving equation (10) for U_{n+1}^c with an approximation for the time derivative

$$\dot{U}^c_{n+1} = \frac{2}{dt_n}(U_{n+1}^c - U_n) - \dot{U}_n. \qquad (14)$$

The local time truncation error at step $n + 1$ for this scheme is

$$d_{n+1} = U_{n+1}^c - U(n + 1) = \tfrac{1}{12}(dt_n)^3\dddot{U}_{n+1} + O(dt_n)^4 \qquad (15)$$

where $U(n + 1)$ is the exact solution at time step $n + 1$. Equations (13) and (15) can be combined to give

$$d_{n+1} = \frac{U_{n+1}^c - U_{n+1}^p}{3(1 + dt_{n-1}/dt_n)} + O(dt_n^4)$$

This result can be used to estimate the next time-step size based on the requirement that a (relative) norm of the error for the next step should be less than a pre-set input value ϵ (Gresho, Lee & Sani 1979)

$$\frac{\|d_{n+2}\|}{\|d_{n+1}\|} = \left(\frac{dt_{n+1}}{dt_n}\right)^3 \frac{\dddot{U}_{n+2}}{\dddot{U}_{n+1}}. \qquad (16)$$

Since $\dddot{U}_{n+2} = \dddot{U}_{n+1} + O(dt_n)$, equation (16) permits the solution for the next potential time step dt_{n+1} after setting $\|d_{n+2}\| = \epsilon$ and neglecting higher-order terms, i.e.

$$\frac{dt_{n+1}}{dt_n} = \left(\frac{\epsilon}{\|d_{n+1}\|}\right)^{1/3} = SFAC.$$

At each time step the factor *SFAC* is computed and if *SFAC* > 1, the next time increment dt_n is increased by *SFAC*, and if *SFAC* < 1, it is decreased by *SFAC*. However, in case *SFAC* becomes too large, we set another criterion *SFAC* $\leqslant$ 2 to avoid overshoot of the solution at dt_{n+1} (Kheshgi & Scriven 1984).

3.3.3. *Iteration scheme*

The global matrix equation (10) is assembled from the element contributions via the frontal solution technique (Irons 1970; Hood 1976; Rast 1994), and a Newton–Raphson scheme is used to solve equation (10) for U_{n+1}. That is, we solve the nonlinear algebraic equations

$$\frac{\partial R_{n+1}(U_{n+1}^j, U_n)}{\partial U_{n+1}^j}\Delta U_{n+1} \simeq -R_{n+1}(U_{n+1}^j, U_n) \tag{17}$$

where j is the iteration number at time step $n + 1$, and

$$\Delta U_{n+1} = U_{n+1}^{j+1} - U_{n+1}^j$$

is used to update U_{n+1} during the iterations. Solution at time step $n + 1$ is obtained when both

$$\max|U_{n+1}^{j+1} - U_{n+1}^j| \leqslant \epsilon \tag{18}$$

and

$$\max|R_{n+1}| \leqslant \epsilon \tag{19}$$

are satisfied. U_{n+1}^{j+1} is then used as the solution U_{n+1} for this time step.

This scheme is very efficient and cost-saving. It has a good convergence rate at each time step and allows reasonable time increments. Note that here we use the same error tolerance ϵ for both time and space. If we choose ϵ to be 10^{-5}, then 1–7 Newton–Raphson iterations (depending on the parameter values for the case investigated) are required at each time step to achieve convergence. For higher tension and smaller Reynolds number, only one Newton–Raphson iteration is required.

The computational cost is nevertheless still huge, especially when a time-dependent oscillating flow is pursued after steady flow has broken down. One typical parameter case which covers the time history of $t = 0$ to $t = 100$–150 requires about 400–800 time steps for the self-excited oscillation to develop. Each time step on average needs about 15–30 CPU minutes on a Silicon Graphics Challenge XL at Leeds University Computing Service CIF3, and about 10-15 CPU minutes on the Supercomputer Fujistu VPX 240/10 at Manchester Computing Centre.

3.4. *Computational accuracy*

The numerical code has been tested for steady flows by (*a*) comparing with results from different methods (Lowe, Luo & Rast 1995), and (*b*) comparing with an analytical model and experiments (Luo & Pedley 1995). It has been checked again here, using our typical grid in which 5060 six-node triangular elements with 10603 nodes are allocated as shown in figure 2, that numerical solutions of a desired accuracy can be obtained, which are independent of the element mesh should the element number be increased. In other words, extensive work has been done to check the spatial accuracy of the solutions. We have confirmed that, in cases for which the time-dependent code leads to a steady solution, the steady membrane shape is graphically indistinguishable from that obtained previously (see figure 20*a* below).

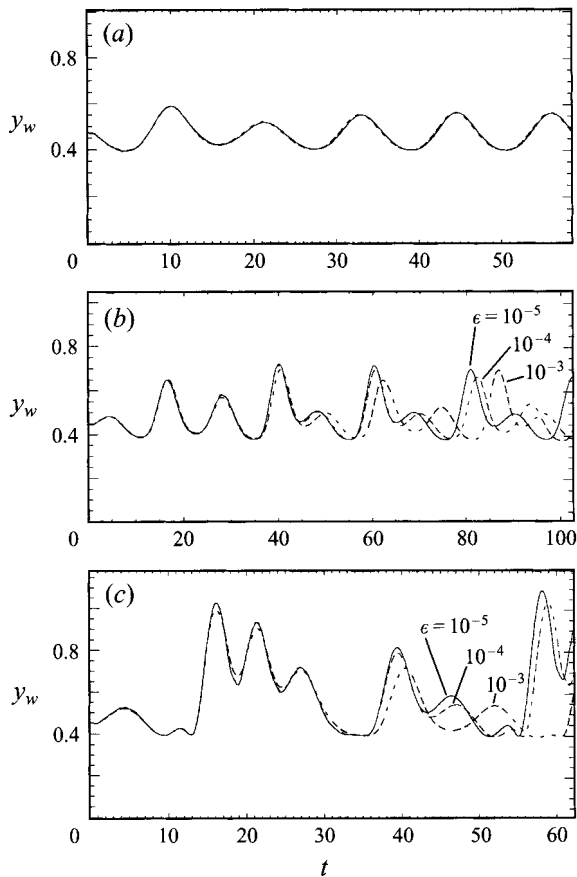It still remains to check the temporal accuracy of the solution. This is controlled

FIGURE 3. Wall position y_w at $x_w = 8.5$ is plotted as a function of time with error tolerance $\epsilon = 10^{-3}$ (short-dashed), $\epsilon = 10^{-4}$ (long-dashed) and $\epsilon = 10^{-5}$ (solid), for (a) case I; (b) case II; and (c) case III.

by the error tolerance ϵ. We have checked for different values of ϵ in the range of $10^{-3} - 10^{-5}$. Results are considered to be reliable when they become independent of ϵ. It should be mentioned here that, although the so-called one-step Newton iteration method, which takes only one iteration for equation (17) and ignores the error thereafter during that time step, has been used successfully for other time-dependent problems (Gresho et al. 1979; Kheshgi & Scriven 1984), we found that for the present problem it is vital to achieve convergence properly within each time step, i.e. to ensure that conditions (18) and (19) are both satisfied. Failure to do so can not only lead to a very small time increment dt_n, hence much smaller t for given computing time, but also causes deviation from the correct solutions. This is especially true when calculating the self-excited oscillations with large amplitude as discussed below.

We have checked that results obtained for many cases are independent of ϵ once $\epsilon \leqslant 1 \times 10^{-3}$. Such an example is shown in figure 3(a), where the wall motion y_w at $x_w = 8.5$ is plotted as a function of time for $\epsilon = 10^{-3}$, $\epsilon = 10^{-4}$, and $\epsilon = 10^{-5}$.

However, this is not the case when the system becomes highly unstable and sensitive to small disturbances, such as cases II and III (defined in §4.3 below). For these cases, wall motions start to diverge from each other after a certain time when different

values of ϵ are chosen. Figure 3(b) shows the calculated oscillations for case II for $\epsilon = 10^{-3}, 10^{-4}$, and 10^{-5}, respectively. Within a limited length of time, solutions obtained for these ϵ are quite close to each other. However, beyond that time, say $t > 35$, the result for $\epsilon = 10^{-3}$ deviates from those for $\epsilon = 10^{-4}$ and 10^{-5}. And for $t > 55$, results at $\epsilon = 10^{-4}$ and 10^{-5} also start to differ. The situation becomes even worse for case III, figure 3(c).

These findings are consistent with the general fact that, if a system is highly dynamic, it is very sensitive to small perturbations. This aspect is discussed further below. Here, if we can make sure that the results obtained for a certain length of time are independent of ϵ, then we can say that the solutions are reliable at least during this time period.

4. Results

4.1. *Parameters*

Following the previous steady flow study (Luo & Pedley 1995), we now investigate the instability of the solutions for the same values of the parameters as used there, namely

$$\mu = 1 \times 10^{-3} \text{ Pa s}, \qquad \rho = 10^3 \text{ kg m}^{-3}, \qquad D = 10^{-2} \text{ m},$$
$$\overline{L} = 5 \times 10^{-2} \text{ m}, \qquad \overline{L}_u = 5 \times 10^{-2} \text{ m}, \qquad \overline{L}_d = 30 \times 10^{-2} \text{ m},$$
$$\overline{P}_d = \bar{p}_e - \bar{p}_d = 0.93 \text{ Pa}, \quad \overline{T}_0 = 1.610245 \text{ N m}^{-1},$$

where $\overline{T}_0$ is the reference value of the tension.

Hence we have, in dimensionless terms, $L_u = 5$, $L = 5$, $L_d = 30$, $D = 1$, $T_0 = 1.610245 \times 10^7 / Re^2$, $P_d = (9.3 \times 10^4 + \triangle p)/Re^2$, $Re = 1 - 500$. The dimensionless parameters T_0 and P_d are dependent on Re because of the non-dimensionlization used in §2.2.

The actual value of dimensionless tension T appearing in equation (3) is given by $T = T_0/\beta$, where β is a parameter ($\geqslant 1$) which is increased in order to investigate the effect of lowering membrane tension. Note that a longer downstream length ($L_d = 30$) is used here than in Luo & Pedley (1995), where $L_d = 7$ was shown to be reasonable for steady flow with a required accuracy. For unsteady flow, however, we choose a much longer downstream length in order to ensure that downstream boundary conditions are properly imposed and to minimize possible wave reflections from the downstream boundary. As a result, an extra term $\triangle p$ estimated from the Poiseuille flow $(= 12(L_d - 7)/ReD)$ is introduced so that we have approximately the same parameters as those in the steady flow study (Luo & Pedley 1995). To test whether the downstream length L_d has any significant effects on the results, especially on the motion of the elastic section during the oscillation, we calculated the oscillation using $L_d = 30$ and $L_d = 32$, respectively, and compared the wall motion y_w (at $x_w = 8.5$) for both values of L_d at $Re = 300$, in figure 4(a) for a regular oscillation, and figure 4(b) for an irregular oscillation.

It is seen from figure 4(a) that the wall motion with the downstream length of $L_d = 32$ seems to have a slightly larger period than that of $L_d = 30$. This is presumably because the longer downstream length increases the downstream resistance and inertance. We have adjusted the downstream transmural pressure P_d assuming that the flow in the additional two units of length is Poiseuille flow, whereas in fact, for flow with Reynolds number as high as 300, and for unsteady cases, the flow at the downstream end is not entirely Poiseuille flow, and therefore has a slightly larger
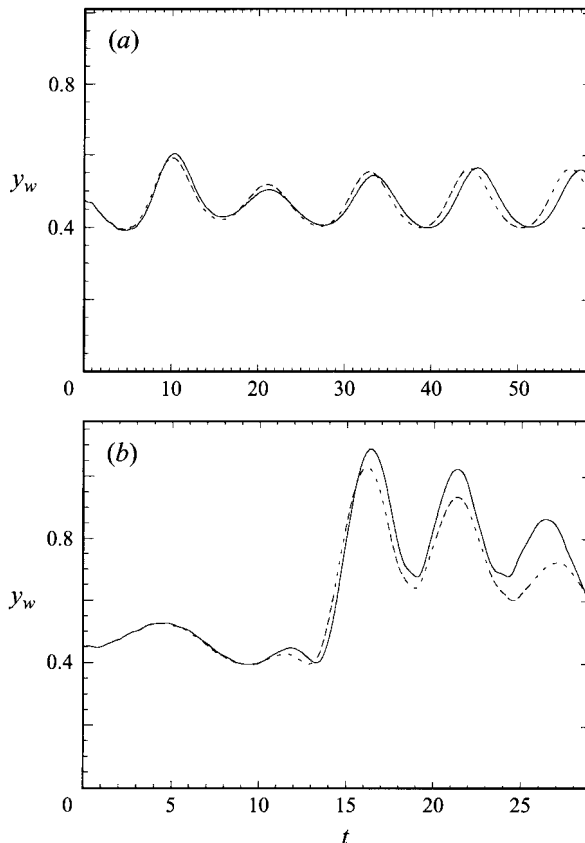
FIGURE 4. Wall position y_w at $x_w = 8.5$ is plotted as a function of time with downstream length $L_d = 32$ (solid) and $L_d = 30$ (dashed), for (a) case I and (b) case II.

resistance than assumed. A greater discrepancy is observed in figure 4(b) which corresponds to case III below, where the oscillation is more irregular, and we therefore know that a small difference in a parameter (resistance or inertance in this case) will inevitably lead to divergent output as time progresses. Despite these aspects, however, we can see that the results remain qualitatively unchanged for the different values of L_d, and we henceforth keep $L_d = 30$.

Several parameters can be varied, namely the Reynolds number Re, the membrane longitudinal tension T, the external pressure with respect to downstream pressure p_d, and the length of the elastic section L. Owing to the extensive computing requirement for the unsteady flow, however, we limit ourselves to investigating cases with different values of Re and T only, while values of P_d and L are fixed. One reason for focusing on the tension parameter is that previous studies have demonstrated breakdown of the steady solution if T becomes small enough (Pedley 1992; Lowe & Pedley 1995; Rast 1994; Luo & Pedley 1995), although as stated above we now believe that in all but the first of these the breakdown was numerical not physical. The other reason is that it was found in our steady flow study (Luo & Pedley 1995) that the effect of increasing P_d is similar to that of lowering T. Morever, in the corresponding one-dimensional analytical model, L can be combined with T in a single dimensionless parameter $\lambda = L/T^{1/2}$ (Luo & Pedley 1995). Extending this finding into two-dimensional flow, we expect the effect of increasing L to be equivalent to that of reducing $T^{1/2}$.
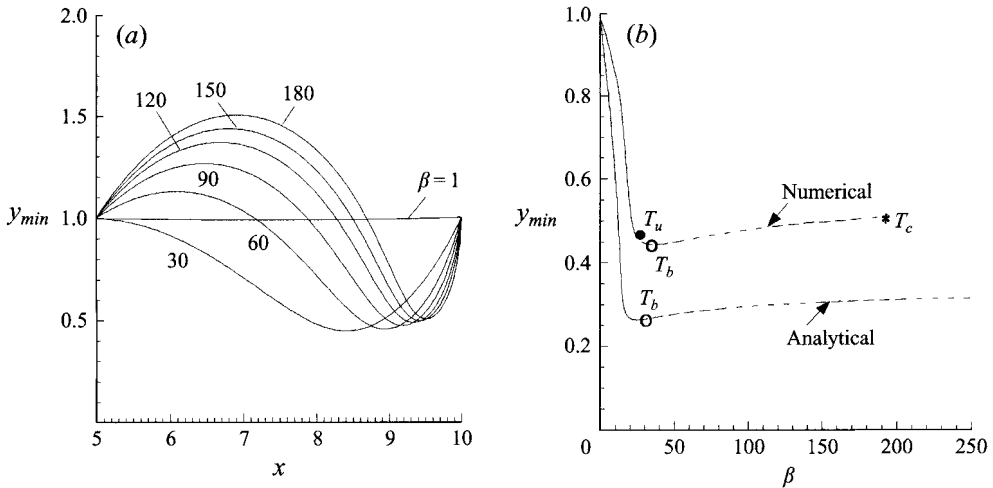
FIGURE 5. Steady solutions at $Re = 300$. (a) The elastic wall shape at different tensions, and (b) the minimum wall postion y_{min} against β, where the upper curve is the numerical result and the lower curve is the prediction from the one-dimensional model (Luo & Pedley 1995). The bulging point T_b is marked as a circle, the unsteady point T_u is marked as a dot, and the critical tension T_c where the numerical scheme broke down is marked as a star.

We have calculated results for different values of Re from 1 to 500, and different values of T. The most interesting results in terms of complicated self-excited oscillations and flow separations, yet still reliable in the sense that all convergence and accuracy checks were satisfactory and the flow remains reproducible, are found at Reynolds numbers of 100–300. To demonstrate the unsteady features, we focus below on the results obtained at $Re = 300$.

4.2. *Instabilities of the steady solutions*

Steady solutions at $Re = 300$ are shown in figure 5(a,b), for $T = T_0/\beta$, where $\beta = 1, 5, 10, \dots 190$ is the reduction factor. For more discussion of these steady solutions, see Luo & Pedley (1995).

A small disturbance is imposed on the steady solution by using a steady solution with a slightly different value of the tension as the initial condition, and the corresponding time-dependent flow is calculated. If the steady solution is stable, the time-dependent flow should eventually approach it. If, instead, the flow deviates from it, then we can say that the steady solution is unstable. By doing this, we are able to show that the steady solutions are stable for $\beta < 27.5$, shown as solid lines in figure 5(b), and (dashed lines) are unstable for $\beta \geqslant 27.5$. Hence the unstable tension is given by $T_u \simeq T_0/27.5$, for $Re = 300$. Values of the corresponding β_u for different Reynolds numbers are listed in table 1 (there was no instability at $Re = 1$). We can see that the unstable tension T_u increases as Re increases. These are accurate within 1.0 (the nearest value of β which was tested and gave stability was $\beta_u - 1.0$). Thus flows of higher Reynolds number are less stable than those of lower Reynolds number for the same tension and transmural pressure; hence both the tension and viscosity in this case are primarily stabilizing factors.

It is noted that the steady solution first becomes unstable at the bottom of the curve in figure 5(b), before the membrane starts to bulge out at the upstream end (Luo & Pedley 1995). The same is true for the other Reynolds numbers investigated here, except $Re = 1$. In other words, steady flow with upstream membrane bulging

$Re=$	1	100	300	400	500
$\beta_u \simeq$		54.0	27.5	20.0	15.0

TABLE 1. Relation of β_u with Re

is unlikely to be stable except perhaps at very small Re. The steady solution shows that, when the membrane bulges out upstream, the pressure drop no longer increases as flow rate increases. In other words, pressure-drop limitation occurs and the curve of pressure drop against flow rate appears to be more or less flat after this point. Not very surprisingly, oscillations have been observed often when pressure-drop limitation is reached in experiments for three-dimensional tube flows (Bonis & Ribreau 1978; Brower & Scholten 1975). This may also explain why such a partly bulged wall shape has not been observed in the experiments that C. D. Bertram has performed (personal communication), though he mainly used thick tubes in his experiments where bending stiffness and inertia of the tube wall may also have played important roles in the onset of the oscillations; morever the fluid flow was turbulent in his experiments.

It would be interesting to perform a stability analysis of the one-dimensional version of this problem, as Jensen did for his similar model of flow in a collapsable tube (Jensen 1990), to compare with our two-dimensional numerical predictions. The disturbances applied here are not necessarily infinitesimal and the time evolutions are nonlinear. Therefore, the instabilities obtained will not be exactly the same as those derived from linear stability theory. Nevertheless, a comparison would help us to understand more of these instabilities and the role that each parameter plays, as well as help us to pick up the parameters corresponding to the most important and interesting flow behaviour more efficiently. Morever, it might save the trouble of an exhaustive parameter search, which we have only been able to begin.

4.3. Self-excited oscillations

After the flow becomes unstable, self-excited oscillations occur. The flow behaviour becomes quite complicated and interesting. We present three cases I, II and III at $Re = 300$, each with a slightly different tension.

(a) Case I: $\beta = 30$

This is the simplest case, in which periodic oscillations are developed for $T < T_u$. The wall position y_w close to the site of maximum deformation, $x_w = 8.5$, is plotted as a function of time t in figure 6(a). The amplitude of this wall motion is nearly 20% of the channel height. The evolution of the elastic wall shape with time during one of the periods, marked as a darker line from (i) to (ii) in figure 6(a), is plotted in figure 6(b). The corresponding wall pressure at $x_w = 8.5$ is also plotted as a function of time in figure 7(a), and the evolution of the pressure drop along the elastic wall is shown in figure 7(b). It is observed that the oscillations of the wall coordinate y_w and wall pressure p_w appear to be roughly in phase. This is due to the fact that there is no energy loss in the wall, and the mass of the membrane is neglected, so that the wall pressure should be in phase with the wall curvature. When the nonlinear term in the wall curvature is small (i.e. when the wall slope is small), the wall curvature has roughly the same phase as the wall coordinate y_w.

The oscillations seems to become quite regular after $t > 20.08$. A fast Fourier transform performed on the traces of figure 6(a) or figure 7(a) gives a fundamental frequency, or Strouhal number, of 0.0838.
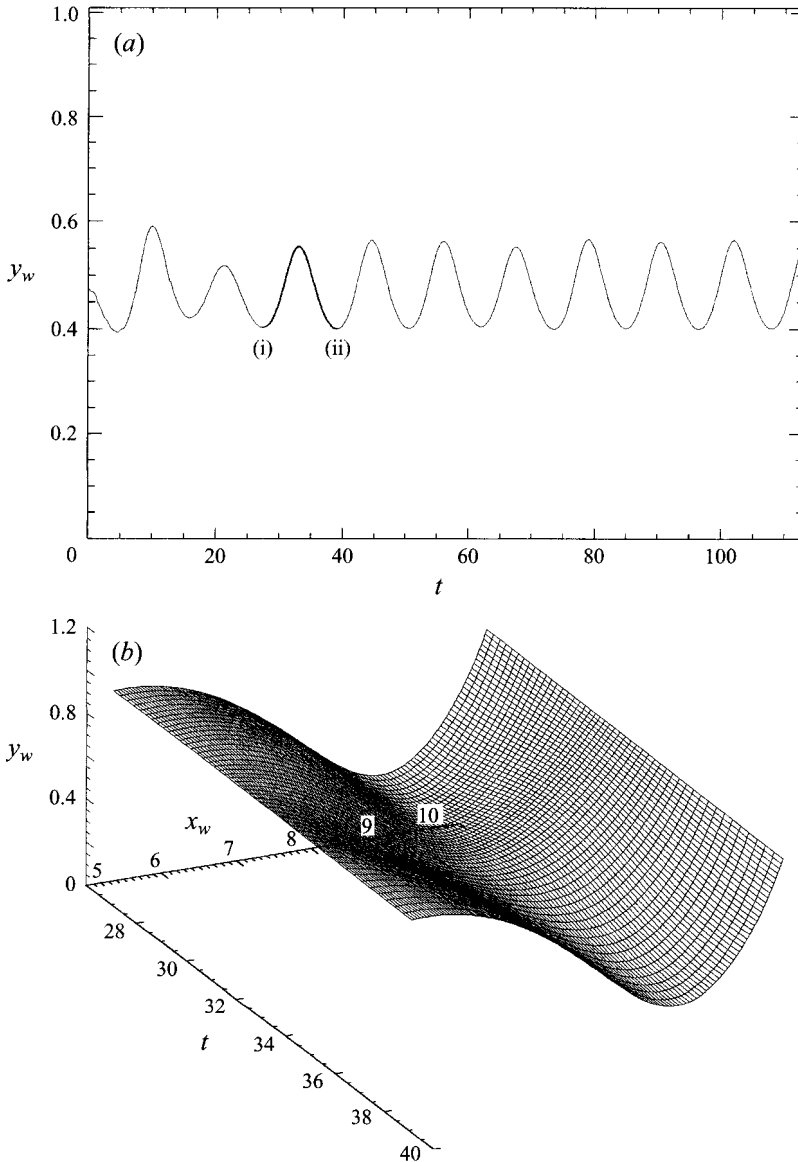
FIGURE 6. Case I: (a) elastic wall position y_w at $x_w = 8.5$ plotted as a function of time; (b) time evolution of the elastic wall shape during the period $t = 27.078$–39.79, marked as darker line from (i) to (ii) in (a).

Streamline plots at different times within an oscillation period are shown in figure 8. It can be seen that flow separation occurs both at the upper corner and on the plane walls of the channel, and several eddies are generated. A vorticity wave is generated downstream of the membrane; the positions of the wave crests and troughs are depicted by A, B, C, and D in figure 8. An 'eddy doubling' appears at the upper corner at time $t = 31.49$. This is very similar to the vorticity wave generated in channel flow with a prescribed moving indentation (Pedley & Stephanoff 1985; Ralph & Pedley 1988, 1989, 1990). The speed of the vorticity wave crest at position B is approximately 0.348, lower than the mean flow velocity, which is one unit.
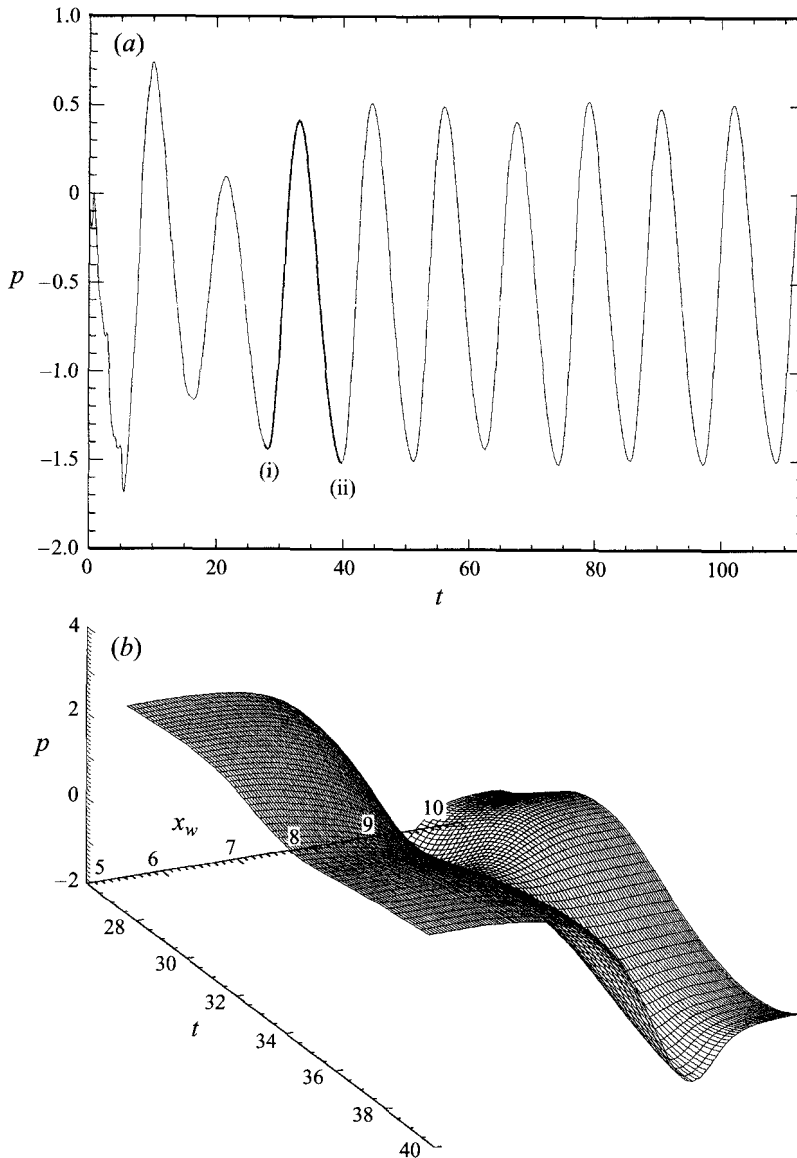
FIGURE 7. Case I: (a) wall pressure at $x_w = 8.5$ plotted as a function of time; (b) time evolution of the pressure distribution along the elastic wall, during $t = 27.0798$–39.1058, marked as darker line from (i) to (ii) in (a).

To compare with the computations of flow with a moving indentation, we plot the positions of wave crests and troughs B, C, and D against the scaled time with respect to the period $t_p \simeq 12.71$, in figure 9. The figure also includes the corresponding plots by Ralph & Pedley (1990, figure 12), for a case in which the wall indentation was given a relatively small oscillation about a mean corresponding to $y_w \simeq 0.6$. Figure 9 shows that these two cases have very similar wave crests and troughs, even though we have different parameters here, $Re = 300$ and $St \simeq 0.0838$ compared with $Re = 500$ and $St = 0.05$ in Ralph & Pedley (1990), and the Strouhal number St is an output for our case as the flow is coupled with the wall motion. It shows that a vorticity
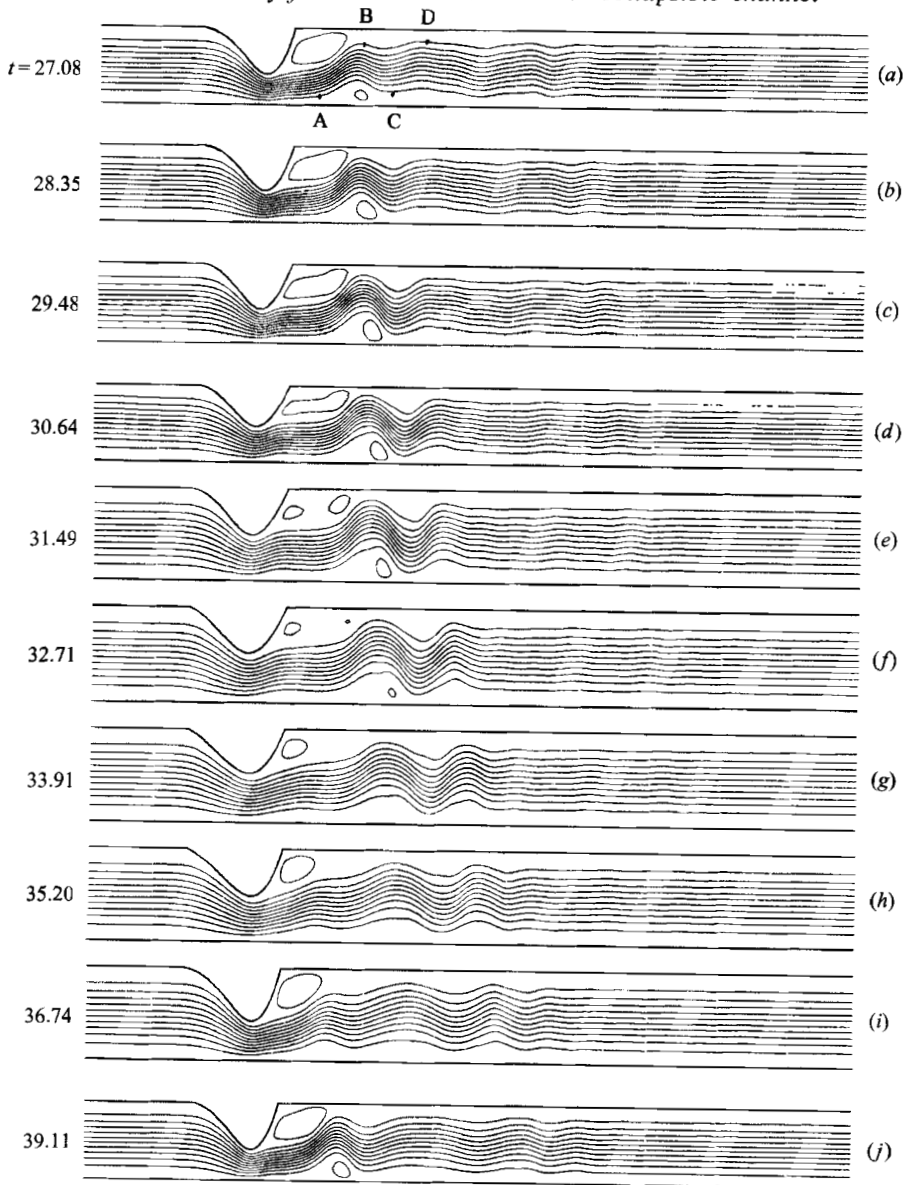
FIGURE 8. Instantaneous streamlines for case I. Up to fifteen equally spaced streamlines are plotted between ψ_{max} and ψ_{min}, during the period $t = 27.08-39.79$: (a) $\psi_{max} = 1.0856$, $\psi_{min} = -0.0217$; (b) $\psi_{max} = 1.0826$, $\psi_{min} = -0.0434$; (c) $\psi_{max} = 1.0699$, $\psi_{min} = -0.0555$; (d) $\psi_{max} = 1.0504$, $\psi_{min} = -0.0471$; (e) $\psi_{max} = 1.0332$, $\psi_{min} = -0.0357$; (f) $\psi_{max} = 1.0181$, $\psi_{min} = -0.0174$; (g) $\psi_{max} = 1.0267$, $\psi_{min} = -0.0052$; (h) $\psi_{max} = 1.0439$, $\psi_{min} = -0.0004$; (i) $\psi_{max} = 1.0690$, $\psi_{min} = -0.0015$; (j) $\psi_{max} = 1.0953$, $\psi_{min} = -0.0368$.

wave is generated in the coupled problem just as in a flow with a prescribed moving indentation.

(b) Case II: $\beta = 32.5$

When tension is reduced slightly, from $\beta = 30$ to $\beta = 32.5$, the oscillations become more complicated. Figures 10(a) and 10(b) are the time history of the wall position
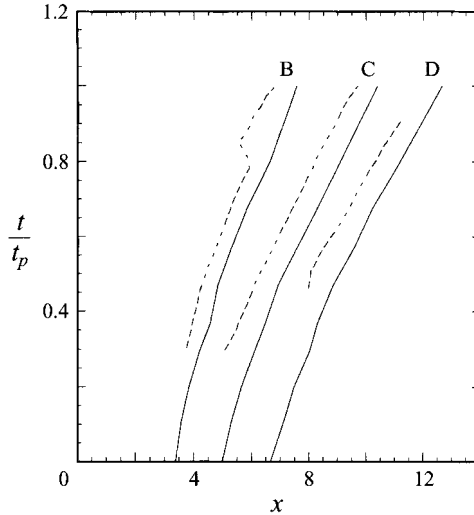
FIGURE 9. Case I, positions of wave crests and troughs B, C, and D plotted against the scaled time t/t_p, where $t_p \simeq 12.03$ is the period: the solid curves are the present computation, and dashed curves are the results obtained by Ralph & Pedley (1990).

y_w at $x_w = 8.5$ and evolution of the wall shape with time for one period, respectively. The corresponding pressure results are plotted in figure 11(*a,b*).

In this case, not only has the amplitude of the wall oscillations increased to about 30% of the channel height, but the wave pattern has changed as well. The overall period t_p has increased to about 20.75. There is alternation between large and small oscillations; and the oscillation is dominated by a slower phase with roughly half of the first fundamental frequency in case I. In other words, the motion appears to have experienced a 'period-doubling bifurcation'.

The streamline contours are shown in figure 12. More eddies are generated along both sides of the channel. At the start, while the pressure at $x = 8.5$ is largest, the eddy immediately downstream of the indentation appears to be enlongated at first, then it splits into two. One of the eddies moves upstream and is dissipated near the membrane, the other propagates downstream and is eventually smeared out there. During the second pressure peak there is only small wall movement, therefore the same eddy stays more or less stationary. It is slightly enlongated at $t \simeq 47.21$, with a possible tendency to split into two, but it returns to its rounder shape at a later time, $t = 49.17$. This shape is retained until the next period starts.

The wave crests and troughs B, C, and D are plotted against time for case II in figure 13. It is seen that the vorticity wave is travelling at a somewhat greater speed than in case I; the average propagation speed of crest B is about 0.527.

(*c*) Case III: $\beta = 35$

As tension is further reduced by increasing β to 35, the wall oscillates violently and rather irregularly, as shown in figures 14 and 15. The amplitude of the oscillations has now increased to be almost 70% of the channel height. There is no evidence of overall periodicity; the 'period' between the two wave 'triples' is about 42.1, suggesting that a further period-doubling bifurcation has occurred, though the shape of the wave form indicates that the bifurcations have greater complexity than simple period-doublings.
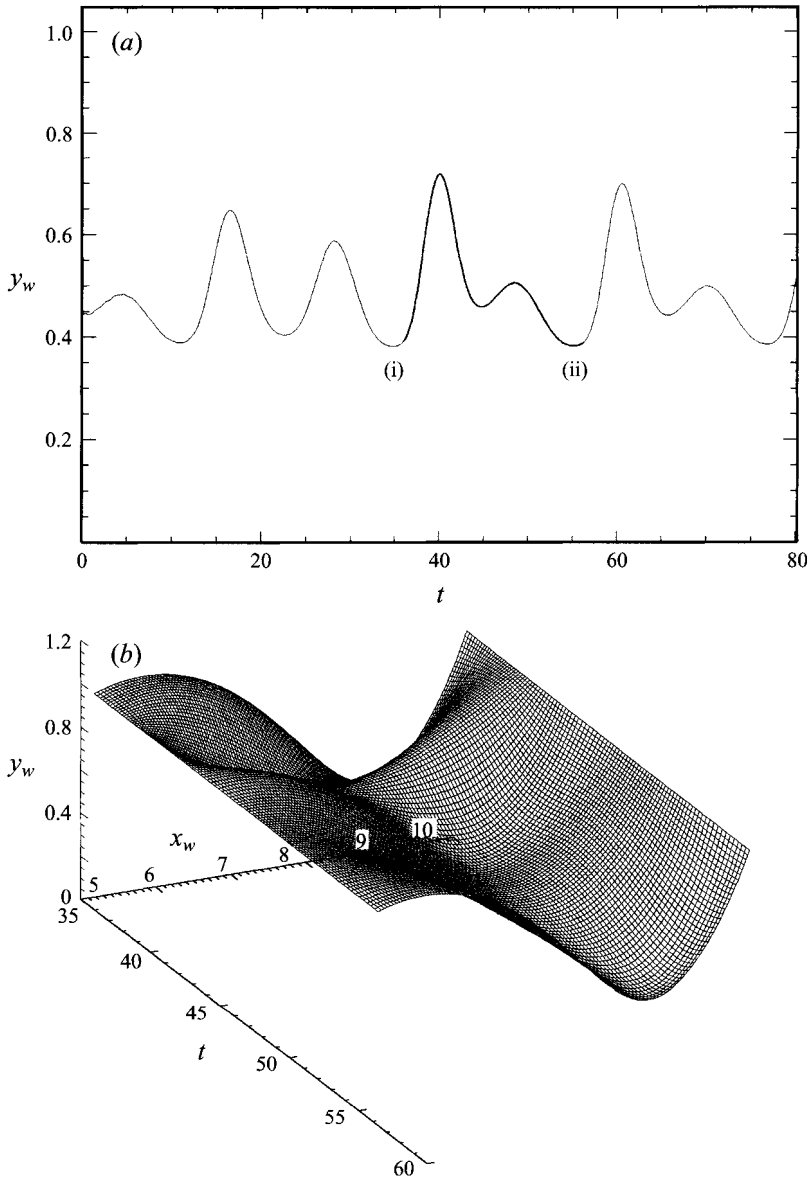
FIGURE 10. Case II: (a) elastic wall position y_w at $x_w = 8.5$ plotted as a function of time; (b) time evolution of the elastic wall shape during the period $t = 35.6$–56.35, marked as darker line from (i) to (ii) in (a).

The streamline plots for case III are shown in figure 16. During the first 'triple-peak' phase, from $t = 11.78$ to 33.99, see figure 16(a–j), several waves, with associated eddies, are generated downstream of the membrane. The sizes and the strengths of the eddies become much bigger than in the previous two cases. The 'eddy doubling' occurs both at the upper corner and on the bottom of the channel. The following double-peak phase, from $t = 33.99$ to 52.99, seems to have kept the character of the double-peak phase of case II, as is shown in figure 16(k–t).

The wave crests and troughs B, C, and D during the first 'triple-peak' phase are plotted against time in figure 17. The average wave speed during this period (at the
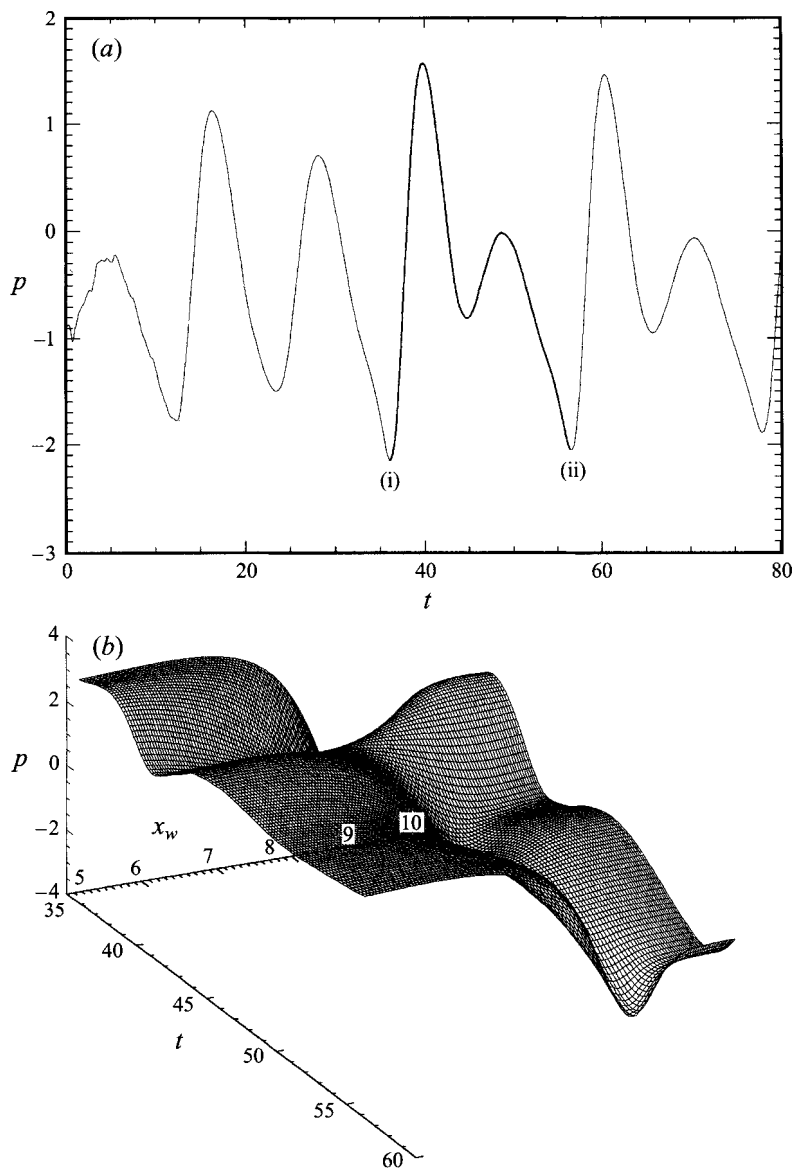
FIGURE 11. Case II: (a) wall pressure at $x_w = 8.5$ plotted as a function of time; (b) time evolution of the pressure distribution along the elastic wall, during the period $t = 35.6$–56.35, marked as darker line from (i) to (ii) in (a).

position B) is about 0.572, though the actual wave speed changes during this phase; the wave travels more slowly during the first peak, then faster during the second peak, and then faster still during the third peak. This is different from cases I and II, see figure 9 and figure 13, where only a small and smooth change in wave speed is seen.

4.4. The sucking phenomenon

When the tension is reduced even further, we have a problem of the wall becoming too soft. The membrane at the downstream end is sucked under the rigid wall so far that it intersects the right-most spine. We cannot yet deal with the problem
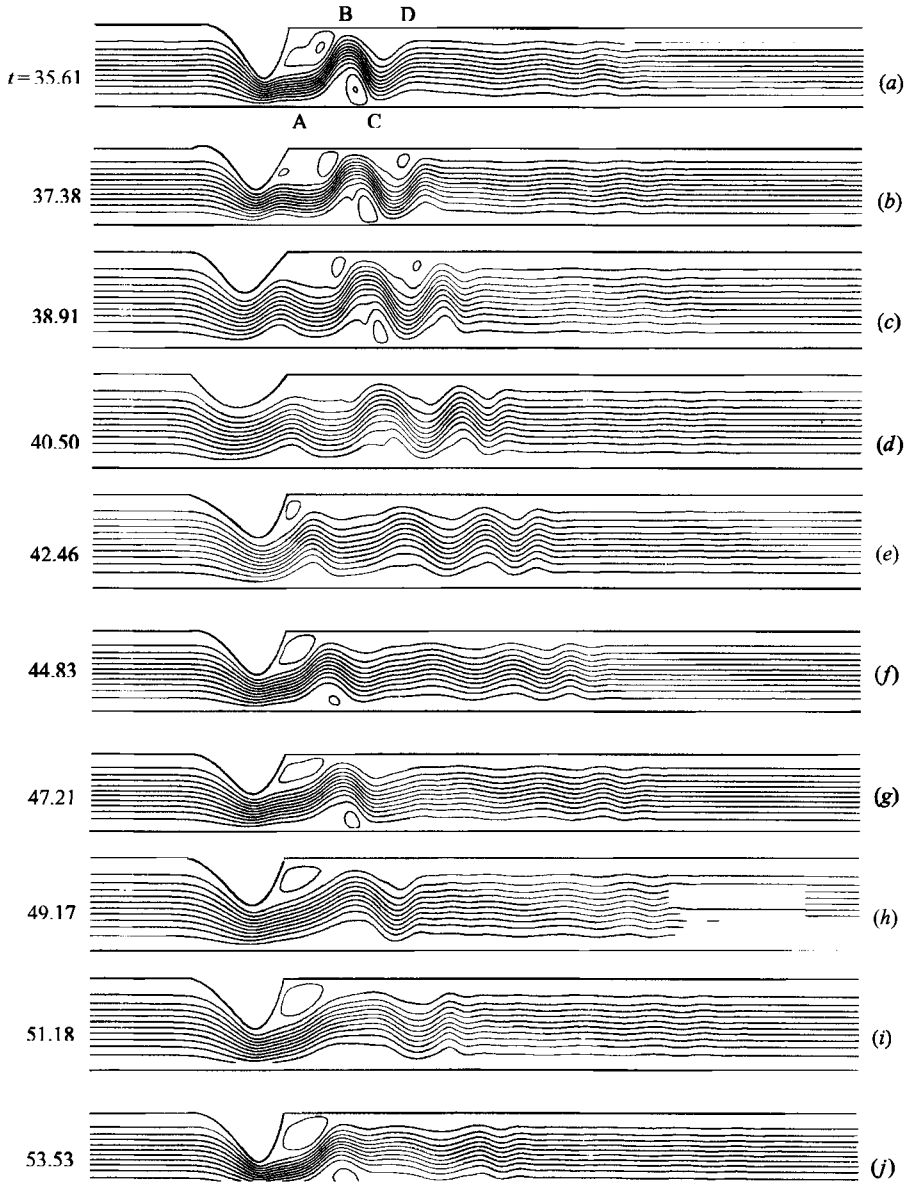
FIGURE 12. Instantaneous streamlines for Case II. Up to fifteen equally spaced streamlines are plotted between ψ_{max} and ψ_{min}, during the 'double-peak' period $t = 35.6$–56.35: (a) $\psi_{max} = 1.0948$, $\psi_{min} = -0.0369$; (b) $\psi_{max} = 1.0838$, $\psi_{min} = -0.0814$; (c) $\psi_{max} = 1.0400$, $\psi_{min} = -0.0434$; (d) $\psi_{max} = 1.0093$, $\psi_{min} = -0.0125$; (e) $\psi_{max} = 1.0310$, $\psi_{min} = -0.0069$; (f) $\psi_{max} = 1.0720$, $\psi_{min} = -0.0192$; (g) $\psi_{max} = 1.0404$, $\psi_{min} = -0.0399$; (h) $\psi_{max} = 1.0364$, $\psi_{min} = -0.0137$; (i) $\psi_{max} = 1.0582$, $\psi_{min} = -0.0040$; (j) $\psi_{max} = 1.0948$, $\psi_{min} = -0.0369$.

when the wall position is multiple-valued, and the numerical scheme therefore breaks down. However, we can observe the early stages of the process since our spines are at an angle to the vertical, as shown in figure 18 for the case $\beta = 50, Re = 300$. Sucking under is also a phenomenon that has been observed in experiments with a thin tube (Ohba *et al.* 1984). It is to avoid the phenomenon that a thick tube
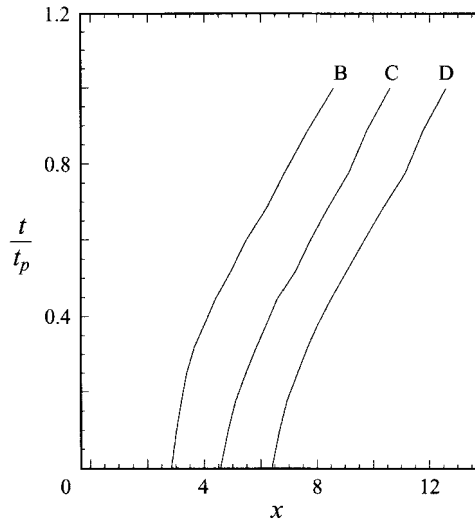
FIGURE 13. Case II, positions of wave crests and troughs B, C, and D plotted against the scaled time t/t_p, where $t_p \simeq 20.49$ is the period.

is preferred in many experiments on flow in collapsible tubes (Bertram 1982, 1986; Bertram *et al.* 1990, 1991).

In principle, it would be possible to simulate the sucking phenomenon by using a more suitable grid. However, the assumption of constant tension in our model is also questionable if the tension is too low. Therefore, a more sophisticated wall model will be required before the sucking phenomenon can be properly investigated. For this reason, we will not pursue it any more in this study.

5. Discussion

5.1. *Justification of the model assumptions*

5.1.1. *The constant tension assumption*

One of the assumptions of this model is that tension remains constant throughout the oscillations. This is problematic since (*a*) there is viscous shear stress which causes the tension to fall with distance along the membrane, and (*b*) the overall membrane length S changes, causing the tension to vary with time. In fact, the tension at position s along the membrane is a function of the membrane length and the shear stress:

$$T = T_0(S) + \int_0^s \sigma_t(\tau) \mathrm{d}\tau \qquad (20)$$

where S is the membrane length, s is the arclength measured from the downstream end, where $T = T_0(S)$, and σ_t is the fluid shear stress in the tangential direction along the membrane.

The second part of equation (20) represents the shear stress contribution, whose effect on the membrane has been investigated in some of the previous steady flow studies (Lowe & Pedley 1995; Rast 1994). It was found, however, that the variation due to shear stress is small compared with the initial tension $T_0(S)$ fixed at the downstream end of the membrane: for the parameter values chosen here, the maximum shear stress contribution is about 5% of $T_0(S)$. Therefore to keep the model simple to start with, it seems reasonable to neglect the shear stress contribution.
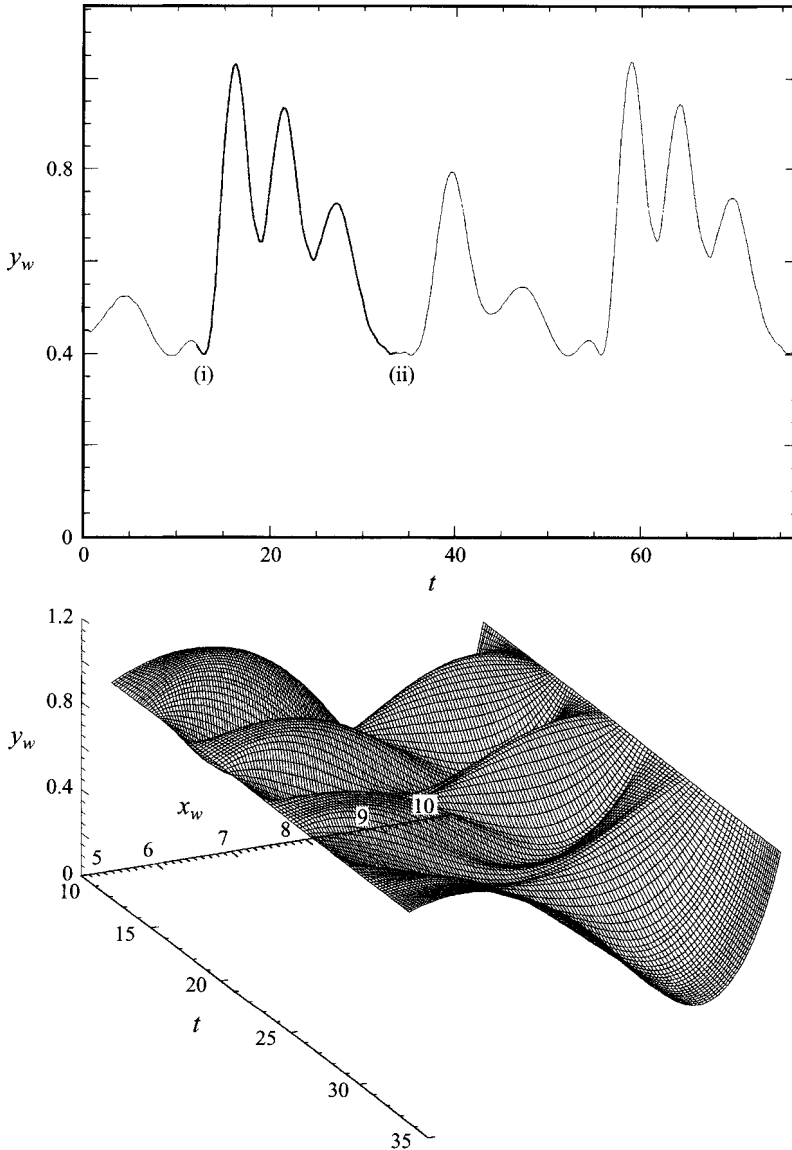
FIGURE 14. Case III: (a) wall position y_w at $x_w = 8.5$ plotted as a function of time; (b) time evolution of the elastic wall shape during the 'triple-peak' phase, $t = 11.79$–33.45, marked as darker line from (i) to (ii) in (a).

The first part $T_0(S)$ of (20) is a function of the membrane length, and it may vary during the oscillations. To assess the validity of neglecting this, we calculated the membrane length variations for the three cases at $Re = 300$, and β=30, 32.5, and 35. Figure 19 shows that the variation $(S - S_0)/S_0$, where S_0 is the initial membrane length at the equilibrium state, is quite small during the oscillations. For case I, where the wall oscillation amplitude is about 20% of the channel height, the maximum variation $(S - S_0)/S_0$ is only 1%. For case II, where a wall oscillation amplitude is about 30% of the channel height, the maximum variation is only about 2%. Even for the most violent oscillation, case III, where the oscillation amplitude is about 70% of the channel height, the maximum variation still remains about 5%. This implies that
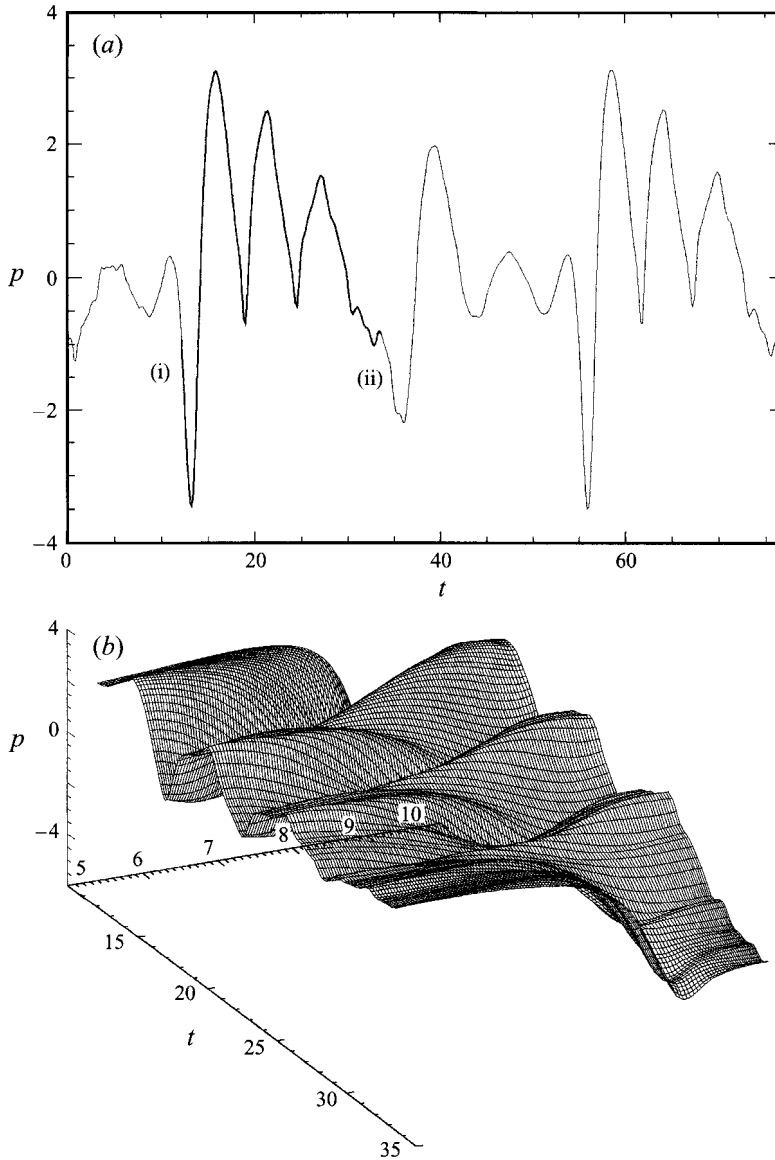
FIGURE 15. Case III: (a) wall pressure at $x_w = 8.5$ plotted as a function of time; (b) time evolution of the pressure distribution along the elastic wall during the 'triple-peak' phase, $t = 11.79\text{--}33.45$, marked as darker line from (i) to (ii) in (a).

the overall variation of tension is within 5% of the initial equilibrium tension T_0 for all our calculations. This should not have significant effect on the basic qualitative features of the system, and hence on the self-excited oscillations illustrated above.

5.1.2. The wall movement assumption

The static membrane equation used in the model determines the equilibrium state of the elastic wall at every time instant; it does not, however, track the movement of individual elements of the wall. In general, if the the wall shape is circular, then a self-consistent wall motion with the constant tension assumption should be one
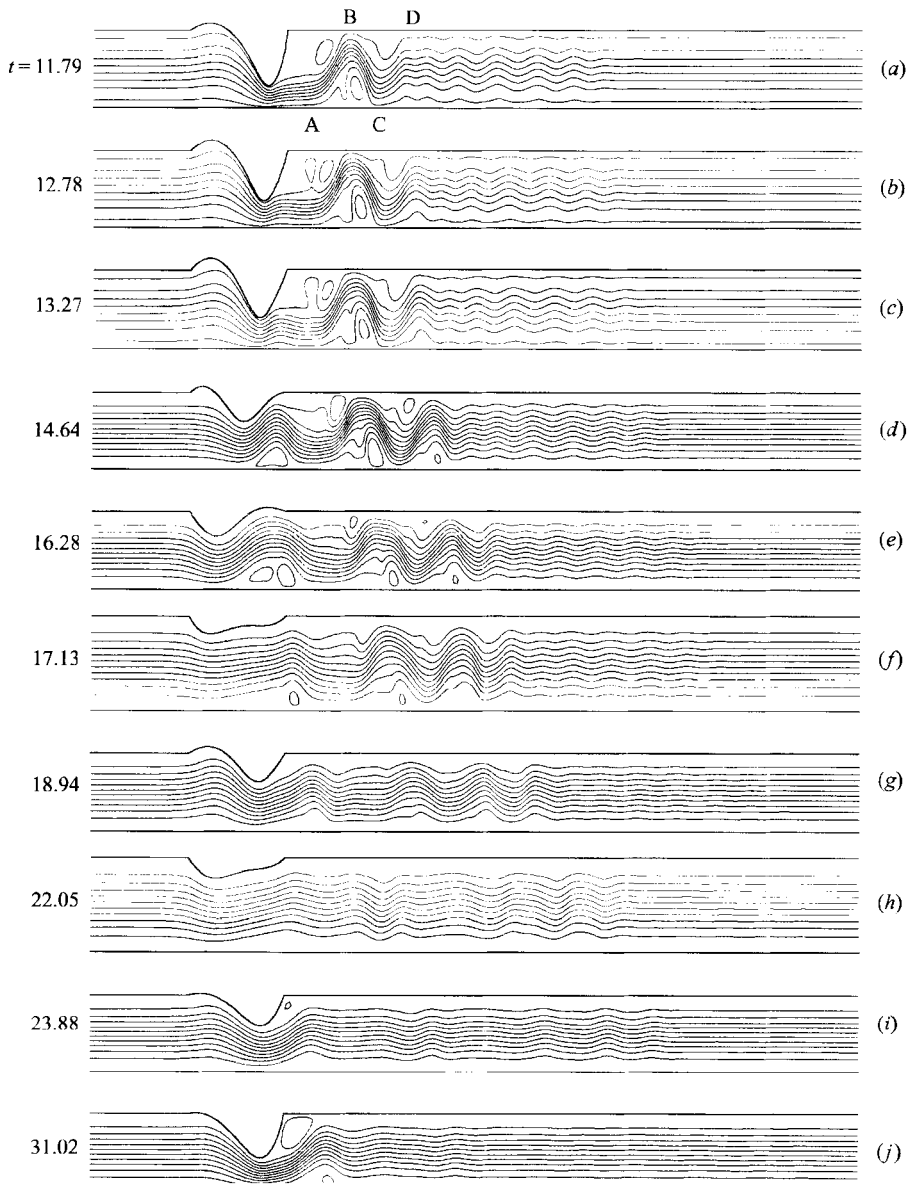
FIGURE 16. Instantaneous streamlines for Case III. Up to fifteen equally spaced streamlines are plotted between ψ_{max} and ψ_{min}, during $(a–j)$ the first 'triple-peak' period and $(k–t)$ the first 'double-peak' period: (a) $\psi_{max} = 1.1708$, $\psi_{min} = -0.1672$; (b) $\psi_{max} = 1.1559$, $\psi_{min} = -0.1631$; (c) $\psi_{max} = 1.1397$, $\psi_{min} = -0.1404$; (d) $\psi_{max} = 1.0856$, $\psi_{min} = -0.0967$; (e) $\psi_{max} = 1.0287$, $\psi_{min} = -0.0694$; (f) $\psi_{max} = 1.0095$, $\psi_{min} = -0.0264$; (g) $\psi_{max} = 1.0027$, $\psi_{min} = -0.0089$; (h) $\psi_{max} = 1.0019$, $\psi_{min} = -0.0010$; (i) $\psi_{max} = 1.0163$, $\psi_{min} = -0.0018$; (j) $\psi_{max} = 1.0888$, $\psi_{min} = -0.0213$.

in which all elements are equally stretched or compressed. This, however, would be difficult to prescribe in advance without knowing the final position of each element, and would require a further round of iterations to achieve.

To apply the no-slip boundary conditions on the membrane, we assumed that the wall is constrained to move in the direction normal to the wall surface, which does represent a self-consistent wall motion when the membrane forms a circular arc. Since
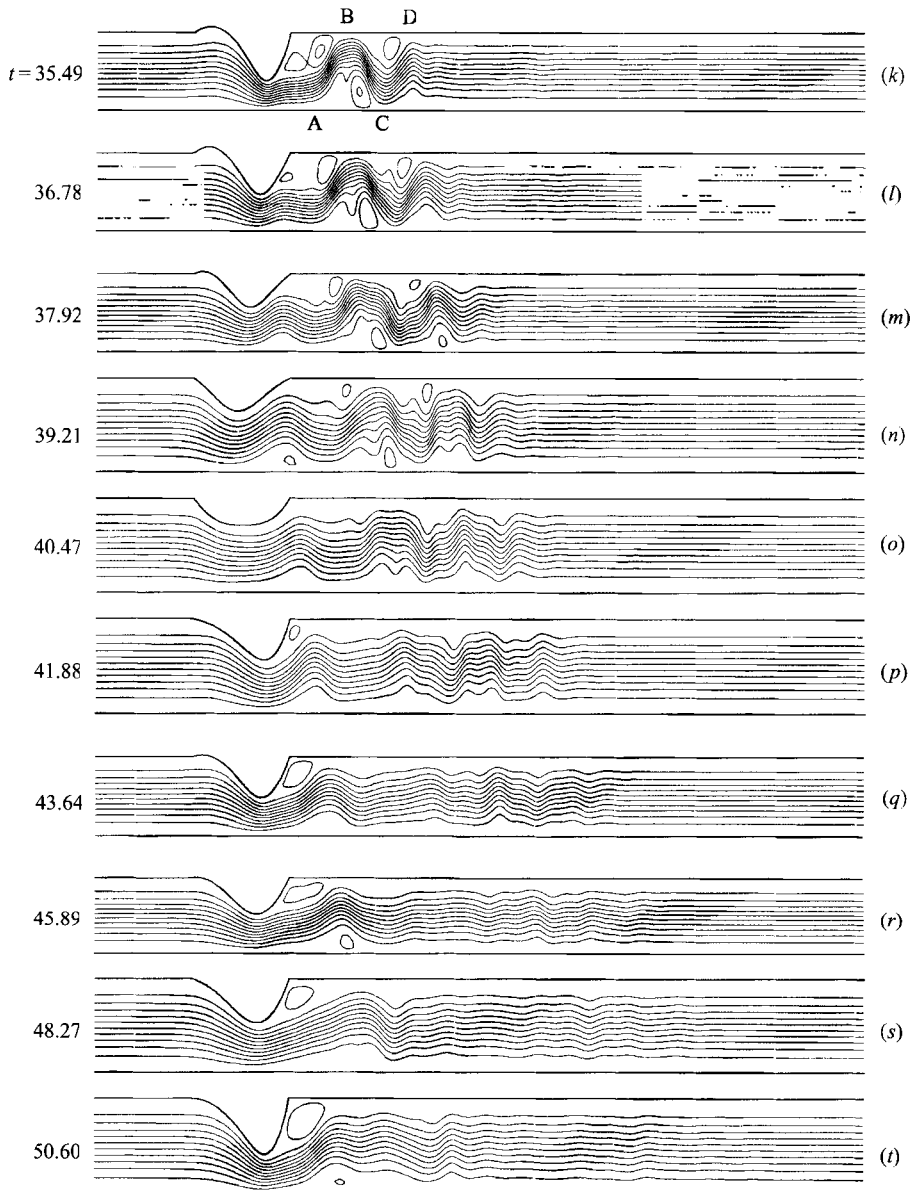
FIGURE 16 (continued). (k) $\psi_{max} = 1.1297$, $\psi_{min} = -0.1155$; (l) $\psi_{max} = 1.0999$, $\psi_{min} = -0.1043$; (m) $\psi_{max} = 1.0602$, $\psi_{min} = -0.0611$; (n) $\psi_{max} = 1.0351$, $\psi_{min} = -0.0371$; (o) $\psi_{max} = 1.0093$, $\psi_{min} = -0.0107$; (p) $\psi_{max} = 1.0237$, $\psi_{min} = -0.0098$; (q) $\psi_{max} = 1.0605$, $\psi_{min} = -0.0081$; (r) $\psi_{max} = 1.0296$, $\psi_{min} = -0.0288$; (s) $\psi_{max} = 1.0355$, $\psi_{min} = -0.0111$; (t) $\psi_{max} = 1.0838$, $\psi_{min} = -0.0158$.

this does not require the final position of the elements to be known, it provides a feasible alternative choice to the wall motion.

One can check whether the choice of wall motion has an important bearing on the oscillations by making a different assumption and comparing the results. The alternative choice made here is that of vertical (y-direction) wall motion. According to linear theory this should give a good approximation to the actual wall motion when the wall slope is small. We therefore compared the wall motions y_w at $x_w = 8.5$
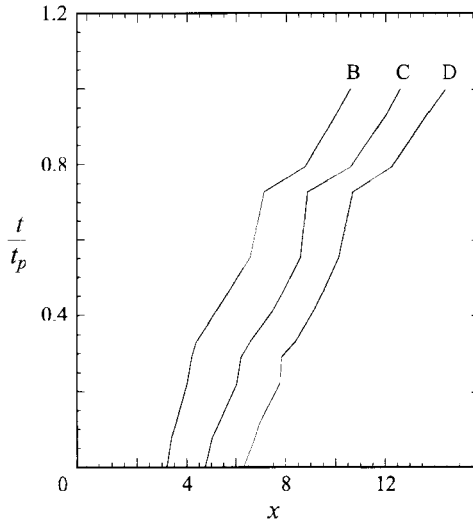
FIGURE 17. Case III, positions of wave crests and troughs B, C, and D plotted against the scaled time t/t_p, where $t_p \simeq 20.54$ is the duration of the 'triple-peak' phase of the oscillation.
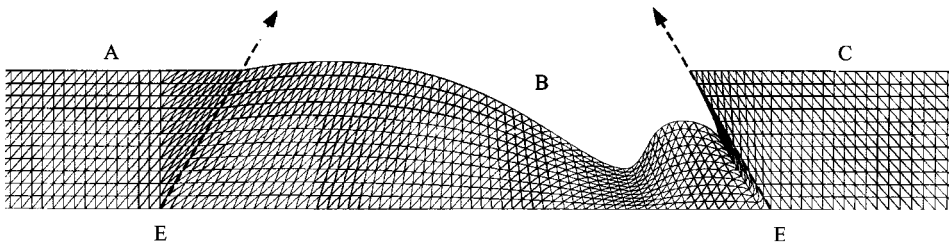

FIGURE 18. Membrane is sucked underneath the rigid wall at the downstream corner and causes the numerical scheme to break down at $Re = 300$ and $\beta = 50$.

obtained from these two assumptions for a case where $T = T_0/25$, $Re = 300$; see figure 20(*a*). In this case, the wall motion approaches its equilibrium position, corresponding to steady flow, in a similar manner for each assumption. We also compared the two results for case I which has a small oscillation amplitude; see figure 20(*b*). Again, the two assumptions lead to very similar wall motions. However, when the wall slope is large, the normal assumption is considered to make more sense than the vertical one. The latter cannot describe, for example, the extreme case when the membrane wall is sucked under the downstream rigid wall, as seen in §4.

Of course, if we wish to understand in more quantitative detail the effects of the assumptions in this subsection and the previous one, §5.1.1, we will need to investigate more realistic wall models for the coupled problem in future.

5.2. *Possible mechanisms of the instability and oscillations: energy dissipation*

Simple models of oscillations in finite-length collapsible tubes, whether lumped (Katz, Chen & Moreno 1969; Schoendorfer & Shapiro 1977; Bertram & Pedley 1982), or one-dimensional (Matsuzaki & Fung 1979; Cancelli & Pedley 1985; Matsuzaki & Matsumoto 1989; Jensen 1990, 1992), have indicated that there must be some mechanism for energy to be dissipated as the flow passes the time-dependent indentation. If the fluid mechanics were purely inviscid there would be no mechanism for the collapse of a massless membrane, once begun, to be halted and reversed, and there
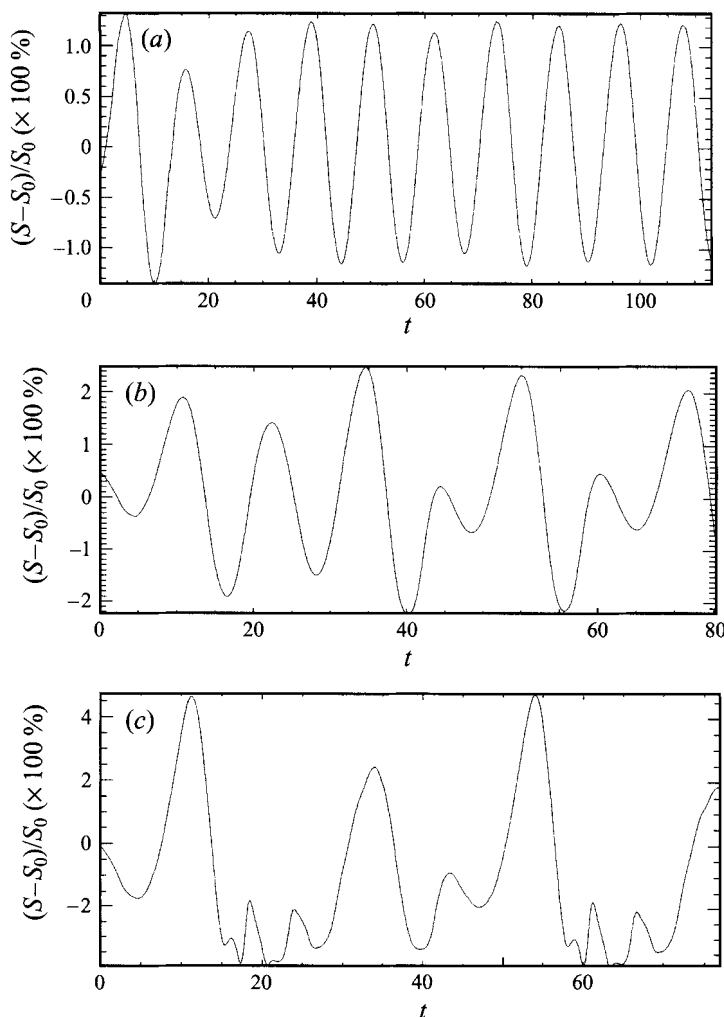
FIGURE 19. The variation of the overall membrane length, $(S - S_0)/S_0 \times 100\%$, during the oscillations for (a) case I, $S_0 = 5.17509$; (b) case II, $S_0 = 5.18890$; and (c) case III, $S_0 = 5.19018$.

would be complete collapse to zero cross-section. We are interested in the principal site of such energy loss in the present case.

Vorticity waves are generated in all cases of self-excited oscillation, and appear to be very similar to those obtained by Ralph & Pedley (1990) in channel flow with a prescribed indentation. This strongly suggests that the movement of the wall itself, whether self-excited or prescribed, is responsible directly for the presence of vorticity waves in the channel downstream. At first sight this also suggests that energy transfer into the vorticity waves might be the required dissipative process. However, the mechanism of wave generation can be shown to be an essentially non-viscous consequence of the displacement of a non-uniform vorticity distribution (Pedley & Stephanoff 1985; Ralph & Pedley 1989), and attempts to couple the inviscid description of the waves to displacements of an elastic membrane have failed to produce oscillations (Borgas 1986; L. Nicolas, private communication).

The process of flow separation from a constriction in a tube at high Reynolds number does lead to substantial energy loss, a crude model of which has formed the basis
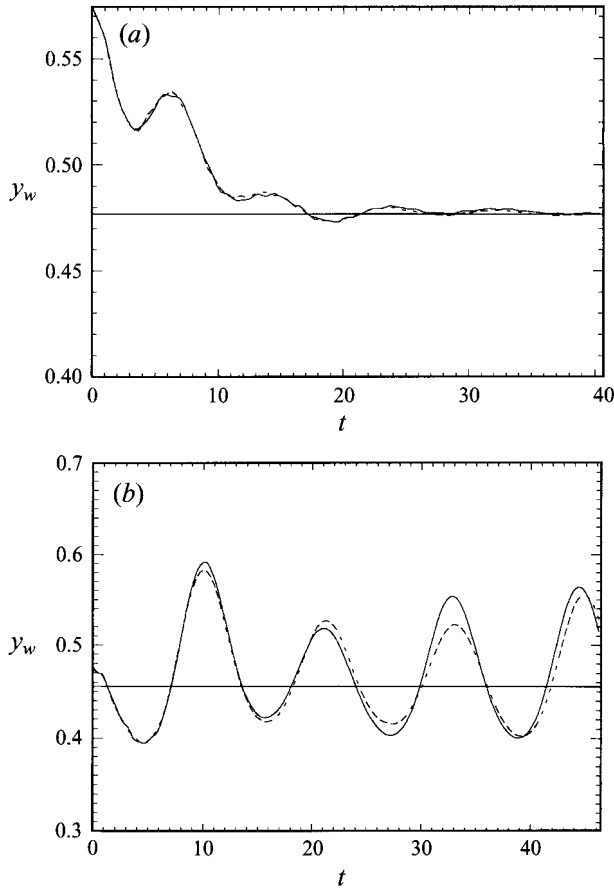
FIGURE 20. Comparison of wall positions y_w at $x_w = 8.5$ obtained from the normal wall motion assumption (solid) and vertical wall motion assumption (dashed), for (a) $\beta = 25$, $Re = 300$; and (b) $\beta = 30$, $Re = 300$. The horizontal lines are the corresponding steady solutions.

of successful models in the lumped or one-dimensional category (e.g. Schoendorfer & Shapiro 1977; Cancelli & Pedley 1985; Matsuzaki & Matsumoto 1989; Jensen 1990, 1992). Examination of the streamline plots in figures 8, 12, and 16 of this paper shows that the flow does indeed separate from the constriction. However, these plots also reveal that the point of flow separation varies very considerably during the oscillations, especially for larger amplitudes (figures 12, 16), and does not always occur at (or just downstream of) the point of minimum cross-section as it would in steady flow and as assumed in the above simplified models. Sometimes, indeed, the flow is not separated anywhere on the indentation even when it is quite large (e.g. figure 16, $t = 16.28$), whereas at other times it does separate from the narrowest point (figure 16, $t = 11.79$, 31.02). Morever, there does not seem to be a simple phase lag between indentation height and separation point, as suggested by experiments on impulsively started flow (Bertram & Pedley 1983). This suggests to us that there may be a coupling between the phase of the vorticity wave and the position of the separation point, and hence perhaps to the energy dissipation required for the membrane oscillations.

We have used our numerical results for $Re = 300$ to compute the rate of viscous energy dissipation per unit volume, $\Phi = (u_{i,j} + u_{j,i})^2/2Re$, at each point in the flow domain at a number of times throughout the computation. The greatest local values

of Φ generally occurred in the thin boundary layers on the two channel walls in the neighbourhood of and upstream of the narrowest point. However, moderately high values were also seen in various places downstream, in the shear layer at the edge of the primary separation zone and on the channel walls near the crests and troughs of the vorticity wave. To see which should be regarded as dominant, we present the results in the form of volume integrals of Φ over the whole channel cross-section and over two ranges of x-values: $5 \leqslant x \leqslant 8.5$, representing the flow under the constriction as far as (approximately) the narrowest point, and $8.5 \leqslant x \leqslant 20$, representing the flow downstream of the narrowest point, including the strongest vorticity waves. To see that this does not give undue prominence to the downstream section, note that in steady flow the upstream section has over 10 times more dissipation than the downstream section (see the horizontal lines on figure 21).

The dissipation values as functions of time are given for case I ($\beta = 30$) in figure 21(a); the times chosen correspond to the oscillation cycle for which the streamlines are shown in figure 8. We see that in this case the upstream dissipation sites dominate the downstream throughout the cycle, but that at the times when the total dissipation is greatest, the downstream section contributes a greater proportion. We note that there is a slight delay between the time of greatest constriction and that of maximum dissipation, but for these gentle oscillations the boundary-layer dissipation wins.

The corresponding results for cases II and III ($\beta = 32.5$ and 35.0) are shown in figures 21(b) and 21(c); the times chosen are those for which streamlines are presented in figures 12 and 16(a–j). There are two things to notice in particular: (i) phases of the motion exist for which the downstream dissipation exceeds the upstream, and (ii) the dissipation is far from quasi-steady. In this case the separated-flow dissipation is important. It is clear that the boundary layers, the unsteady separation and the link to the vorticity waves need a much more detailed investigation.

It would be desirable to relate the instability found here to previous models of boundary-layer instability over infinitely long compliant walls (Carpenter & Garrad 1986; Carpenter & Morris 1990; Weaver & Paidoussis 1977; Grotberg & Reiss 1984; Grotberg & Shee 1985; Lucey & Carpenter 1992; Davies 1995; Davies & Carpenter 1995, 1996). Apart from Tollmien–Schlichting waves, which occur when the boundaries are rigid, the two main types of such boundary-layer instabilities are: divergence, which occurs in the form of a stationary or very slowing moving wave when the wall stiffness is unable to balance the perturbation pressure exerted by the fluid; and travelling-wave flutter, which typically has phase speeds close to the free-stream velocity and is associated with an irreversible energy transfer from the fluid to the wall. However, the oscillation in our model normally occurs at a velocity well below any of the critical velocities of those flow-induced instabilities, as calculated by Davies & Carpenter (1995, 1996), for example. This is not too surprising since the critical velocities were calculated using linear theory for a basic flow with zero mean pressure gradient in an infinitely long channel with compliant walls which are parallel (Davies 1995; Davies & Carpenter 1995, 1996). Probably the most significant difference in our case is the fact that the steady state is one in which the membrane is already significantly deformed, so even for infinitesimal disturbances, analysis of the instability requires the time-dependent perturbation of separated flow. In addition, the membrane in our case has no mass and the tension is constant, meaning that there could not be an irreversible energy transfer from the fluid to the membrane, thus precluding travelling-wave flutter. Tollmien–Schlichting waves are known to cause instability only when interacting with a travelling-wave flutter or on their own at very high Reynolds number (where $Re \sim 8000$, C. Davies, personal
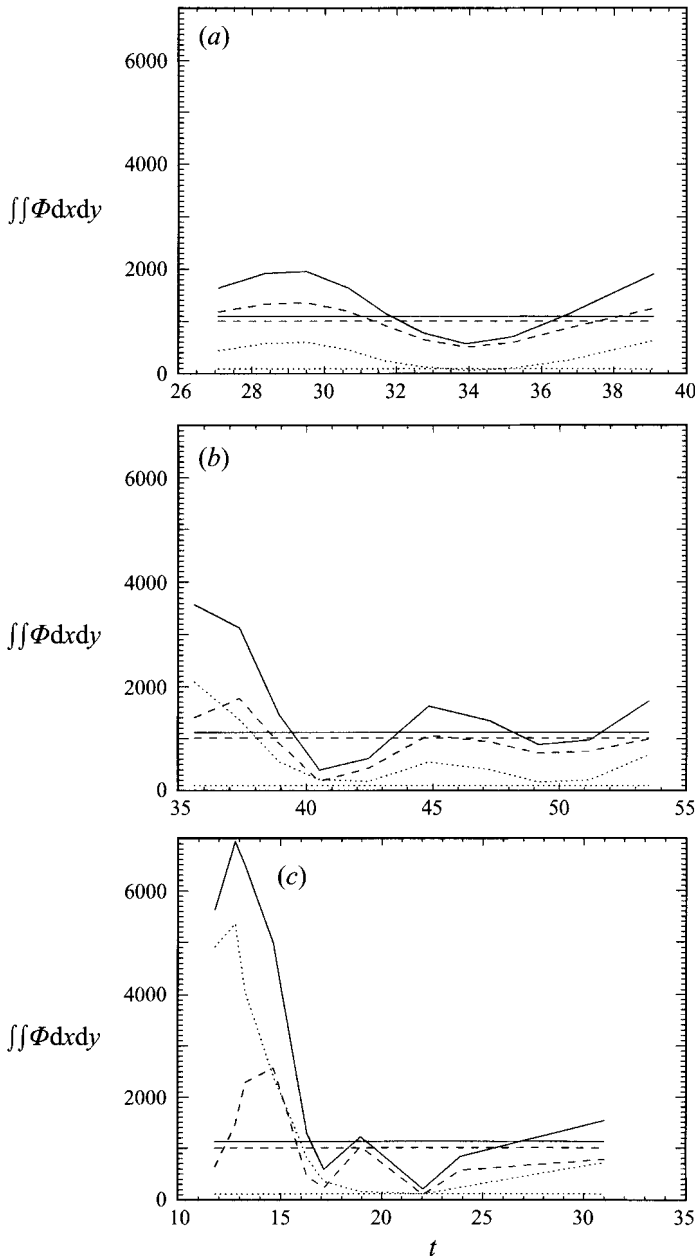
FIGURE 21. The volume integrals of Φ over the whole channel cross-section $\int_0^1 \int_5^{20} \Phi \, \mathrm{d}x\mathrm{d}y$(solid curve); the upstream section $\int_0^1 \int_5^{8.5} \Phi \, \mathrm{d}x\mathrm{d}y$ (dashed curve); and the downstream section $\int_0^1 \int_{8.5}^{20} \Phi \, \mathrm{d}x\mathrm{d}y$ (dotted curve), for (a) case I ($\beta = 30$), (b) case II ($\beta = 32.5$), and (c) case III ($\beta = 35$). The horizontal lines represent the energy dissipation integrals obtained from the corresponding steady solutions.

communication). Therefore they are highly unlikely to be relevant in the cases studied here. Qualitatively, though, we might be able to explain the oscillation in case I (see §4.3), in terms of a divergence instability. However, the bifurcations and nonlinear evolution of cases II and III cannot be explained using linear stability theory.

Finally, it should be remembered that channel flow instabilities become three-

dimensional at sufficiently large Reynolds number and sufficiently far downstream from the initial disturbance (e.g. Orszag & Patera 1983), and there is no reason to doubt that the same will be true for flow in a collapsible channel. Certainly the vorticity waves observed by Stephanoff & Pedley (1985) became three-dimensional far downstream. Therefore even a complete survey of the present two-dimensional model will not give the whole picture, especially when it is remembered that most experiments are performed on collapsible *tubes*.

5.3. *Chaos?*

It is still an open question whether the dynamical system represented by flow through a compressed elastic tube of finite length is one that gives rise to chaotic behaviour. Such behaviour is certainly indicated by the (turbulent) experiments (Bertram 1982, 1986; Bertram *et al.* 1990, 1991) although chaos could not be certainly identified because of the limited lengths of recording made in the experiments, and by the one-dimensional model of Jensen (1992). We too are limited in the lengths of time for which the computations could be run. However, strong evidence for chaos in our numerical simulation comes from the dependence of the long-time wall motions on the tolerance level ϵ (see §3.4 and figure 3). Further numerical investigation is clearly required.

5.4. *Comparison with experiment*

It is desirable to compare our results with experimental measurements. However, a direct comparison is not feasible since no experimental data are available in the literature for flow in a two-dimensional collapsible channel. Nevertheless, there are indirect experimental observations in tubes which may support the predictions here. First, the location of the calculated unstable points seems to agree with the experimental observations of the conditions at which steady flow gives way to self-excited oscillations in tubes (see figure 2 in Bertram *et al.* 1990; Bertram 1982; Bonis & Ribreau 1978; Luo & Pedley 1995), as we have discussed in §4.2. Second, the wall and pressure oscillation patterns, with 'double-peak' and 'triple-peak' phases, look analogous to the recordings of the tube area and pressure in the experiments by Bertram *et al.* (1990), and by Bertram (1982). These also include apparent chaos as the oscillation becomes more complicated (Bertram *et al.* 1991). Third, the vorticity waves generated downstream have similar features to those observed in the case of a prescribed indentation, which have been visualized in experiments (Pedley & Stephanoff 1985). The wave speed is also comparable to the speed of the indentation-flow vorticity wave; see figure 9. And finally, when the tension is too low, implying a very thin membrane, we have the membrane sucking, which agrees with experimental observations in very thin tubes (Ohba *et al.* 1984). Thus many features of the oscillations predicted are consistent with a variety of experiments.

6. Conclusion

A time-dependent code has been developed using a simultaneous approach and an adaptive mesh to solve the flow–membrane interaction problem. The stability of the steady solutions from our previous study (Luo & Pedley 1995) is investigated by simulating the unsteady flow after applying a small perturbation to these solutions.

For small Re, the unsteady flow approaches the corresponding steady flow for all values of tension and external pressure that were studied, i.e. the steady solutions for small Re are stable. For moderate Re ($Re = 100 - 500$), however, the unsteady flow approaches the steady flow only if T is large enough. If T is smaller than T_u

($\beta > 27.5$ for $Re = 300$, say), then the steady solution becomes unstable. The unstable tension T_u increases with Re, and is smaller than (but quite close to) the bulging tension T_b (Luo & Pedley 1995) in all the cases studied. For all Re in the 'moderate' range, self-excited oscillations were found for $T < T_u$. The flow patterns become increasingly complicated as tension is decreased from T_u. There is a lower value of T below which the amplitude of the membrane motion becomes very large and the membrane tends to be sucked underneath the rigid wall downstream. This sucking phenomenon has been observed in experiments on thin tubes (Ohba *et al.* 1984).

The present simulation provides a good opportunity to look at the details of the flow pattern, and should enable us to build up improved analytical models to investigate and understand the physical mechanisms.

The next stage of the numerical work is to improve our model by introducing a properly described wall using beam theory. Ultimately, we would also like to see whether a fully coupled, three-dimensional model will give similar results. Before that, however, we have already shown that a rich variety of self-excited oscillations exists even over a small parameter range for this two-dimensional model problem based on very simple wall assumptions.

REFERENCES

BERTRAM, C. D. 1982 Two modes of instability in a thick-walled collapsible tube conveying a flow. *J. Biomech.* **15**, 223–224.

BERTRAM, C. D. 1986 Unstable equilibrium behaviour in collapsible tubes. *J. Biomech.* **19**, 61–69.

BERTRAM, C. D. & PEDLEY, T. J. 1982 A mathematical model of unsteady collapsible tube behaviour. *J. Biomech.* **15**, 39–50.

BERTRAM, C. D. & PEDLEY, T. J. 1983 Steady and unsteady separation in an approximately two-dimensional indented channel. *J. Fluid Mech.* **130**, 315–345.

BERTRAM, C. D., RAYMOND, C. J. & PEDLEY, T. J. 1990 Mapping of instabilities for flow through collapsed tubes of different length. *J. Fluids Struct.* **4**, 125–154.

BERTRAM, C. D., RAYMOND, C. J. & PEDLEY, T. J. 1991 Application of nonlinear dynamics concepts to the analysis of self-excited oscillations of a collapsible tube conveying a fluid. *J. Fluids Struct.* **5**, 391–426.

BONIS, M. & RIBREAU, C. 1978 Etude de quelques propriétés de l'écoulement dans une conduite collabable. *La Houille Blanche* **3/4**, 165–173.

BORGAS, M. S. 1986 Waves, singularities and non-uniqueness in channel and pipe flows. PhD thesis, Cambridge University.

BROWER, R. W. & SCHOLTEN, C. 1975 Experimental evidence on the mechanism for the instability of flow in collapsible vessels. *Med. Biol. Engng* **13**, 839–845.

CANCELLI, C. & PEDLEY, T. J. 1985 A separated-flow model for collapsible-tube oscillations. *J. Fluid Mech.* **157**, 375–404.

CARPENTER, P. W. & GARRAD, A. D. 1986 The hydrodynamic stability of flow over Kramer-type compliant surfaces. Part 2. Flow-induced surface instabilities. *J. Fluid Mech.* **170**, 199–232.

CARPENTER, P. W. & MORRIS, P. J. 1990 The effect of anisotropic wall compliance on boundary-layer stability and transition. *J. Fluid Mech.* **218**, 171–223.

DAVIES, C. 1995 Evolution of Tollmien-Schlichting waves over a compliant panel. PhD thesis, University of Warwick.

DAVIES, C. & CARPENTER, P. W. 1995 Numerical simulation of the evolution of Tollmien-Schlichting waves over finite compliant panels. *J. Fluid Mech.* (submitted).

DAVIES, C. & CARPENTER, P. W. 1996 Instabilities in a panel channel flow between compliant walls. to be submitted.

EHRENSTEIN, U. & KOCH, W. 1989 Three-dimensional wavelike equilibrium states in plane Poiseuille flow. *J. Fluid Mech.* **228**, 111–148.

ENGELMAN, M. S., SANI, R. L. & GRESHO, P. M. 1982 The implementation of normal and/or tangential boundary conditions in finite element codes for incompressible fluid flow. *Intl J. Numer. Meth. Fluids* **2**, 225–238.

GRESHO, P. M., LEE, R. L. & SANI, R. L. 1979 On the time-dependent solutions of the Navier-Stokes equations in two and three dimensions. In *Recent Advances in Numerical Methods in Fluids* (ed. C. Taylor & K. Morgan), pp. 27–79.

GROTBERG, J. B. & REISS, E. L. 1984 Subsonic flapping flutter. *J. Sound Vib.* **92**, 349–361.

GROTBERG, J. B. & SHEE, T. R. 1985 Compressible-flow channel flutter. *J. Fluid Mech.* **159**, 175–193.

HOOD, P 1976 Frontal solution program for unsymmetric matrices. *Intl J. Numer. Meth. Engng* **10**, 379–399.

IRONS, B. M. 1970 A frontal solution program for finite element analysis. *Intl J. Numer. Meth. Engng* **2**, 5–32.

JENSEN, O. E. 1990 Instabilities of flow in a collapsed tube. *J. Fluid Mech.* **220**, 623–659.

JENSEN, O. E. 1992 Chaotic oscillations in a simple collapsible tube model. *J. Biomech. Engng* **114**, 55–59.

KATZ, A. I., CHEN, Y. & MORENO, A. H. 1969 Flow through a collapsible tube. *Biophys. J.* **9**, 1261–1279.

KHESHGI, H. S. & SCRIVEN, L. E. 1984 Penalty finite element analysis of unsteady free surface flows. *Finite Elements in Fluids* **5** 393–434.

KRAMER, M. O. 1962 Boundary layer stabilization by distributed damping. *J. Am. Soc. Naval Engrs* **74**, 341–385.

LOWE, T. W., LUO, X. Y. & RAST, M. P. 1995 A comparison of three solution methods for flow in a collapsible channel. *J. Fluids Struct.* (submitted).

LOWE, T. W. & PEDLEY, T. J. 1995 Computation of Stokes flow in a channel with a collapsible segment. *J. Fluids Struct.* **9**, 885–905.

LUCEY, A. D. & CARPENTER, P. W. 1992 A numerical simulation of the interaction of a compliant wall and inviscid flow. *J. Fluid Mech.* **234**, 147–170.

LUO, X. Y. & PEDLEY, T. J. 1995 A numerical simulation of steady flow in a 2-D collapsible channel. *J. Fluids Struct.* **9**, 149–174.

MATSUZAKI, Y. & FUNG, Y. C. 1979 Nonlinear stability analysis of a two-dimensional model of an elastic tube conveying a compressible flow. *J. Appl. Mech.* **46**, 31–36.

MATSUZAKI, Y. & MATSUMOTO, T. 1989 Flow in a two-dimensional collapsible channel with rigid inlet and outlet. *J. Biomech. Engng* **111**, 180–184.

OHBA, K., YONEYAMA, N., SHIMANAKA Y. & MAEDA, H. 1984 Self-excited oscillation of flow in collapsible tube. *Tech. Rep. Kansai Univ.* **25**, 1–13.

ORSZAG, S. A. & PATERA, A. T. 1983 Secondary instability of wall-bounded shear flows. *J. Fluid Mech.* **128**, 347–385.

PEDLEY, T. J. 1992 Longitudinal tension variation in collapsible channels: a new mechanism for the breakdown of steady flow. *J. Biomech. Engng* **114**, 60–67.

PEDLEY, T. J. & STEPHANOFF, K. D. 1985 Flow along a channel with a time-dependent indentation in one wall: the generation of vorticity waves. *J. Fluid Mech.* **160**, 337–367.

RALPH, M. E. & PEDLEY, T. J. 1988 Flow in a channel with a moving indentation. *J. Fluid Mech.* **190**, 87–112.

RALPH, M. E. & PEDLEY, T. J. 1989 Viscous and inviscid flows in a channel with a moving indentation. *J. Fluid Mech.* **109**, 543–566.

RALPH, M. E. & PEDLEY, T. J. 1990 Flow in a channel with a time-dependent indentation in one wall. *J. Fluids Engng* **112**, 468–475.

RAST, M. P. 1994 Simultaneous solution of the Navier-Stokes and elastic membrane equations by a finite-element method. *Intl J. Numer. Meth. Fluids* **19**, 1115–1135.

REYN, J. W. 1974 On the mechanism of self-excited oscillations in the flow through collapsible tubes. *Delft Prog. Rep.* **1**, 51–67.

RILEY, J. J., GAD-EL-HAK, M. & METCALFE, R. W. 1988 Compliant coatings. *Ann. Rev. Fluid Mech.* **20**, 393–420.

RUSCHAK, K. J. 1980 A method for incorporating free boundaries with surface tension in finite element fluid-flow simulators. *Intl J. Numer. Meth. Engng* **15**, 639–648.

SAITO, H. & SCRIVEN, L. E. 1981 Studying of coating flow by the finite element method. *J. Comput. Phys.* **42**, 53–76.

SCHOENDORFER, D. W. & SHAPIRO, A. H. 1977 The collapsible tube as a prosthetic vocal source. *Proc. San Diego Biomed. Symp.* **16**, 349–356.

SHAPIRO, A. H. 1977 Steady flow in collapsible tubes. *J. Biomech. Engng* **99**, 126–147.

SILLIMAN, W. J. 1979 Viscous film flows with contact lines. PhD thesis, University of Minnesota.

WEAVER, D. S. & PAIDOUSSIS, M. P. 1977 On collapse and flutter phenomena in thin tubes conveying fluid. *J. Sound Vib.* **50**, 117–132.